Computer Methods in Applied Mechanics and Engineering 444 (2025) 118100

Contents lists available at ScienceDirect

Comput. Methods Appl. Mech. Engrg.

journal homepage: www.elsevier.com/locate/cma

Enhancing dynamic modeling of porous media with compressible fluid: A THM material point method with improved fractional step formulation

Jidu Yu [a], Weijian Liang [b], Jidong Zhao [a,*]

[a] Department of Civil and Environmental Engineering, Hong Kong University of Science and Technology, Kowloon, Hong Kong, China
[b] Department of Civil and Environmental Engineering, Hong Kong Polytechnic University, Kowloon, Hong Kong, China

ARTICLE INFO

Keywords:
Multiphysics coupling
Material point method
Large deformation
Fractional step method
Compressible fluid
Wave propagation

ABSTRACT

Modeling dynamic behavior and large deformation in porous media, encompassing coupled fluid flow, solid deformation, and heat transfer, remains a critical challenge in geomechanics. While the two-phase material point method (MPM) combined with the semi-implicit fractional step method (FSM) has demonstrated efficacy for saturated porous media under large deformation, traditional FSM is constrained to incompressible fluid and divergence-free velocity condition, limiting their applicability to scenarios involving compressible fluids, such as unsaturated soils or thermo-active systems. This study presents an enhanced FSM-based MPM framework that incorporates fluid compressibility and thermal expansivity under non-isothermal conditions. Key innovations include a node-based implicit scheme to solve intermediate variables, significantly improving computational efficiency while maintaining stability. Through a suite of hydro-mechanical (HM) and thermo-hydro-mechanical (THM) coupling benchmarks, we demonstrate that fluid compressibility is essential for FSM to accurately resolve pressure shock waves induced by mechanical or thermal loading. Temporal resolution critically influences modeling of wave dynamics, with larger time steps accelerating wave attenuation. Notably, the semi-implicit FSM can achieve comparable accuracy to explicit schemes while offering superior stability in dynamic regimes, irrespective of fluid compressibility. Practical trade-offs between computational efficiency and pressure wave-capture fidelity are discussed, guiding method selection based on scenario-specific needs. Furthermore, we explore the framework's potential extension to triphasic porous systems to highlight its versatility for geomechanical applications. The work bridges a critical gap in simulating compressible, multiphysics-coupled porous media, offering a robust tool for both academic and industrial challenges.

1. Introduction

The interplay of fluid flow, solid deformation, and heat transfer within porous media, collectively referred to as coupled hydro-mechanical (HM) and thermo-hydro-mechanical (THM) phenomena, occurs frequently in geological and geotechnical engineering. Modeling these intricately intertwined phenomena is often challenging due to the interdependence of multiple physical fields. Traditional mesh-based numerical techniques, particularly the finite element method (FEM), have advanced significantly in addressing TH and THM-coupled conditions. Contemporary geotechnical design emphasizes the need for comprehensive control

* Corresponding author.
E-mail addresses: jyubu@connect.ust.hk (J. Yu), weijian.liang@polyu.edu.hk (W. Liang), jzhao@ust.hk (J. Zhao).

https://doi.org/10.1016/j.cma.2025.118100
Received 16 January 2025; Received in revised form 21 April 2025; Accepted 13 May 2025
Available online 4 June 2025

and prediction of geostructural behavior across a wide range of strain regimes, from small to large strains and eventual failures [1]. In large deformation scenarios, FEM often struggles with predictive capabilities, primarily due to mesh distortion issues. In response, particle-based and mesh-free methodologies have emerged as compelling alternatives, gaining traction in computational geomechanics over the past two decades. Notable among these methods are particle finite element method (PFEM) [2,3], MPM [4–6], smoothed particle hydrodynamics (SPH) [7–9], reproducing kernel particle method (RKPM) [10,11], and peridynamics [12,13]. Each method has its unique strengths and limitations, with this study focusing specifically on MPM.

MPM is a hybrid Eulerian and Lagrangian method that uses Lagrangian particles, known as material points (MPs), to discretize the material domain, convey material information, and track material movements while employing an Eulerian background mesh to solve the governing equations. Unlike the fixed quadrature in FEM [14], the material points in MPM can move across cell boundaries, and the background mesh is reinitialized after each solution loop. This combination allows MPM to leverage the advantages of the Lagrangian approach for simulating history-dependent materials while utilizing the Eulerian approach for addressing large-deformation problems. Recent extensions of MPM have addressed the TH and THM problems in porous media [15–23]. The early application of MPM for saturated porous media predominantly employed explicit time integration due to its simplicity and robustness in dynamic scenarios [15–17,20,21,23]. In explicit multiphase MPM formulations, the kinematic variables are solved on the background mesh, while pore pressure is typically computed on the particles. Notably, to facilitate the explicit solution of pore pressure, fluid compressibility or the fluid bulk modulus must be specified. Consequently, the time step size is governed by the fluid compressibility (*e.g.*, about 0.5×10^{-9} Pa^{-1} for water). Some studies mitigate computational overhead by assuming higher compressibility values (*e.g.*, 1×10^{-8} Pa^{-1}), allowing for larger time steps but potentially compromising solution accuracy [22].

Subsequent developments in MPM have introduced fully implicit time integration for HM-coupled problems, eliminating the need to specify fluid compressibility [18,24]. In incompressible HM-coupled formulations, the pore pressure is implicitly solved by ensuring the divergence-free velocity. However, it is known that under incompressible limit or undrained conditions, the pressure field may exhibit unphysical checkerboard modes if equal-low order interpolation functions are used for both the pressure and velocity fields in coupled MPM. This stability issue, known as inf-sup instability, is inherent to the mixed formulation and is also encountered in other numerical methods, including FEM. A common approach to mitigate unphysical pressure oscillations is to set the interpolation order for the velocity fields one order higher than that of the pressure field. However, this adjustment inevitably alters the existing MPM formulation and increases computational costs [25]. To maintain the use of low-order interpolation functions while ensuring stability, several techniques have been introduced to stabilize the pressure field, including reduced integration [24], node- and/or element-based averaging method [16], polynomial pressure projection [26,27], variational multiscale method [28,29], and fractional step method [19]. Among these, the fractional step method is particularly notable for balancing stability, efficiency, and accuracy without introducing additional stability parameters, thereby gaining popularity within the MPM community [30–35].

The fractional step method (FSM), also known as the projection method, was originally proposed by Chorin [36] to solve the incompressible Navier–Stokes equations. It has been widely recognized for its efficacy in stabilizing pressure field, even though it does not always satisfy the inf-sup condition, as later studies have shown [37,38]. Central to the FSM is the decoupling of pressure and kinematic variables in momentum equations via intermediate velocities. Although initially developed for fluid dynamics, the FSM has proven equally effective when applied to saturated porous media [39–42]. Recently, Kularathna et al. [19] incorporated the FSM into a one-point two-phase MPM to model HM-coupled large-deformation behavior in saturated porous media. Instead of enhancing stability, the semi-implicit time integration in this implementation alleviates the constraints imposed by fluid compressibility and permeability conditions on the time step size. Furthermore, the FSM-based semi-implicit MPM framework has been extended to THM problems in porous media experiencing large deformations, such as permafrost thawing [43], and has recently been applied to simulate unsaturated soils [35], although the compressibility of the gas phase was not considered in that study.

In existing FSM-based MPM studies, the compressibility of fluid (liquid and/or gas) was typically not considered [19,30,31,34,35]. While the incompressible fluid assumption is manageable for most saturated porous media, it may lead to considerable errors when dealing with those containing highly compressible fluids, such as unsaturated soils, gas-hydrate-bearing sediments, tracer gas flow in porous media, and oil–gas reservoirs [44–46]. In geotechnical engineering, pore gases often exhibit compressibility magnitudes two to four orders greater than those of pore liquids. Even for relatively weakly compressible fluids like water, assuming incompressibility can result in a loss of crucial physical information, including dynamic effects [47], which will be discussed later. Consequently, there is a pressing need to extend the applicability of FSM to cover a broader range of fluid conditions, from incompressible to weakly and highly compressible fluids. However, a significant concern arises regarding the feasibility of utilizing the FSM for modeling compressible fluids in porous media, given its original development for incompressible fluid. Incorporating a compressibility term in the mass balance equation may disrupt the divergence-free velocity condition. Therefore, before extending the FSM to simulate unsaturated porous media, it is essential to evaluate its performance when considering fluid compressibility in coupled MPM simulations.

To address this concern, the study enhances the original fractional step formulation to accommodate compressible fluid conditions. While the conventional FSM requires matrix treatment and algebraic solution for two linear equation sets, namely the momentum predictor equations and the pressure Poisson equation, these steps remain computationally demanding [34]. To mitigate this, we propose a node-based implicit scheme utilizing lumped matrices to solve the momentum predictor equations, thereby reducing the number of linear system iterations from two to one. A suite of numerical benchmarks further validates the method's accuracy and efficiency for both incompressible and compressible flows. For compressible scenarios, where analytical solutions are unavailable, simulation results are cross-verified against existing FEM data and explicit MPM simulations from the open-source CB-Geo MPM code [48]. The proposed framework employs a single-point, multiphase updated Lagrangian MPM, rigorously tested under isothermal and non-isothermal conditions. Although focused on biphasic saturated porous media, the formulation can be

extended to unsaturated media by modifying density and compressibility parameters to represent a water-air mixture [47]. Finally, the study further explores the method's adaptability to triphasic porous systems with capillary suction, demonstrating its potential for broader applications in geomechanics and multiphase flow.

The structure of the paper is organized as follows. Section 2 will present the governing equations pertinent to THM-coupled problems in porous media with compressible fluid. Section 3 will outline the THM-coupled MPM algorithm based on improved semi-implicit FSM; Section 4 will showcase a range of diverse numerical examples crafted to assess the viability of FSM for handling compressible fluids in porous media. Section 5 will discuss the extension of FSM for triphasic porous media. Finally, Section 6 will provide conclusive summaries of our findings.

2. Governing equations for fluid-infiltrated porous media

This section presents the mathematical model for porous media with compressible fluid under non-isothermal conditions. For generality, we start the derivation of governing equations from triphasic porous media wherein the pore fluid is a mixture of liquid and gas. Then, by assuming homogenized kinematics and material properties for the liquid-gas mixture, the three-phase porous media can be simplified as a two-phase porous medium where the equivalent fluid compressibility can vary significantly. Since this work mainly focuses on the effect of fluid compressibility rather than the theory development for unsaturated soils or multiphase flow in porous media, the capillary suction effect is not included here and will be discussed later in Section 5.

2.1. Homogenization of a triphasic porous medium

We consider the dynamic excitation of a porous medium consisting of a solid skeleton (s) permeated by an interstitial fluid (f), whereas the fluid phase is composed of uniformly distributed liquids (l) and gases (g). Based on the mixture theory [49], each material constituent $\pi = s, l, g$ in a representative volume element (RVE) can be characterized by its volume fraction n_π, which is used to define a partial density quantity ρ^π by weighting the intrinsic density ρ_π. It is also convenient to characterize the volume fraction for the fluid components $\vartheta = l, g$ by the degree of saturation S_ϑ. The volume fraction for each phase and the degree of saturation for fluid components in an RVE are defined and intertwined with the porosity ϕ as follows,

$$n_\vartheta := \frac{dV_\vartheta}{dV} = \phi S_\vartheta, \quad n_s := \frac{dV_s}{dV} = 1 - \phi, \quad S_\vartheta := \frac{dV_\vartheta}{dV_l + dV_g} = \frac{dV_\vartheta}{dV_f} = \frac{n_\vartheta}{n_l + n_g}, \tag{1}$$

where dV and dV_π are the volumes of the RVE and the π phase, respectively, and dV_f is the volume of the fluid. The volume fraction of the fluid phase, which is equal to the porosity, is defined as,

$$n_f := \frac{dV_f}{dV} = \frac{dV_l + dV_g}{dV} = n_l + n_g = \phi. \tag{2}$$

Then, the partial density for each phase can be calculated based on the volume fraction, *i.e.*, $\rho^\pi := n_\pi \rho_\pi$, and the density of mixture is calculated by $\rho_m = n_s \rho_s + n_l \rho_l + n_g \rho_g$.

2.2. Equation of state for fluid and solid phases

For non-isothermal porous media, the density of each phase depends on the thermodynamic conditions, represented by the equation of state (EOS). The EOS is usually material-dependent. Generally, EOS is a function of temperature and pressure, *i.e.*, $\rho_\pi = \rho_\pi(p_\pi, T_\pi)$, where p_π and T_π are the pressure and temperature of π phase, respectively. Since the temperature for all phases is assumed to be uniform, the phase-wise temperature is replaced by a single temperature field T hereafter.

It is more convenient to use the differential form of an EOS, expressed as,

$$\frac{D^\pi \rho_\pi}{Dt} = \rho_\pi \left(\alpha_\pi \frac{D^\pi p_\pi}{Dt} + \beta_\pi \frac{D^\pi T}{Dt} \right), \tag{3}$$

where $D^\pi(*)/Dt$ is the material derivative with respect to π phase, and α_π and β_π are the compressibility and thermal expansivity, respectively, defined as,

$$\alpha_\pi := \frac{1}{\rho_\pi} \frac{\partial \rho_\pi}{\partial p_\pi}, \quad \beta_\pi := -\frac{1}{\rho_\pi} \frac{\partial \rho_\pi}{\partial T}. \tag{4}$$

For solid and liquid phases, α and β are often assumed to be constant, and then Eq. (3) can be integrated into the following exponential form,

$$\rho_\pi = \rho_\pi^0 \exp\left[\alpha_\pi (p_\pi - p_\pi^0) - \beta_\pi (T - T^0)\right], \tag{5}$$

where ρ_π^0 is the reference density at the reference pressure p_π^0 and temperature T^0. The intrinsic density of the solid phase is also a function of the effective stress on the skeleton, but is not considered in this study.

For the gas phase, the classical Peng–Robinson equation [50] offers an accurate prediction of gas state,

$$p_g = \frac{RT}{V_{mg} - b} - \frac{a\alpha}{V_{mg}^2 + 2bV_{mg} - b^2}, \tag{6}$$

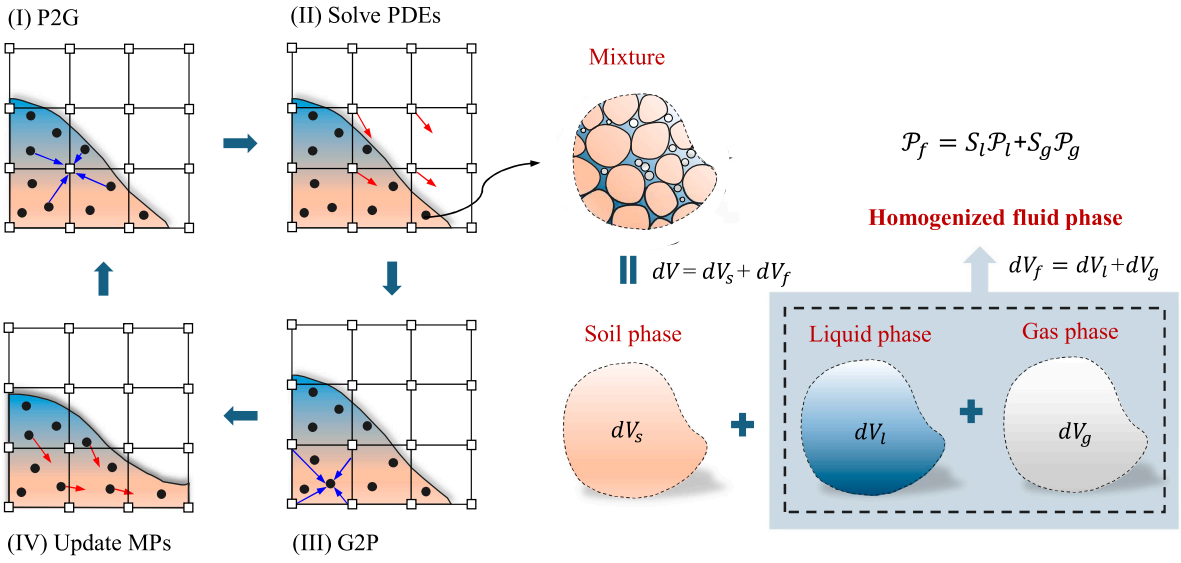

Fig. 1. Illustration of the solution procedure of single-point multiphase MPM and the homogenization of a triphasic porous medium to a biphasic solid–fluid mixture. The MPM solution procedure mainly includes four steps: (1) P2G — map Particle information to Grid; (2) Solve PDEs — solve the governing equations on the background grid; (3) G2P — map Grid information to Particles; (4) Update MPs — update the material point properties and kinematics.

where $V_{mg} = M_g/\rho_g$ is the gas molar volume, M_g is the gas molar mass, R is the gas constant, α is a temperature-dependent function in the equation, a and b are two substance-specific constants calculated using critical properties (temperature and pressure) and the acentric factor of the substance. If a and b are set as zero, the Peng–Robinson equation is reduced to the EOS for the ideal gas, *i.e.*, $\rho_g = M_g p_g / RT$. For simplicity, we use the ideal gas equation in the following work [49,51,52]. Based on Eq. (3), it is easy to find that the compressibility and the thermal expansibility of an ideal gas can be expressed as,

$$\alpha_g = \frac{M_g}{\rho_g RT} = \frac{1}{p_g}, \quad \beta_g = \frac{M_g p_g}{\rho_g RT^2} = \frac{1}{T}. \tag{7}$$

Obviously, the gas compressibility is nonlinearly related to temperature and pressure. Under the normal atmospheric pressure of 101 kPa, the compressibility of gas is approximately 1×10^{-5} Pa^{-1}, which is much larger than that of water, around 0.5×10^{-9} Pa^{-1}.

2.3. Balance equations for triphasic porous media

The balance equations for the considered porous media are formulated in the single-point multiphase MPM framework, as illustrated in Fig. 1.

2.3.1. Mass balance equations

In the single-point multiphase MPM, all phases are represented by a shared Lagrangian material point in the current configuration. In this framework, solid phase motion dictates the movement of the material points, while fluid phases move relative to the solid phase, governed by Darcy-type flow or similar constitutive laws. Mass conservation of the solid phase is automatically fulfilled, as the material point trajectory follows solid motion. For the fluid phase, the local fluid mass can change due to fluid migration and solid deformation. Global mass conservation, however, is rigorously enforced via the mass conservation equation for each phase. Assuming no mass exchange between phases and no external sources, the mass balance equations for the solid and the fluid phases in the Lagrangian frame are given by,

$$\frac{D^s[(1-\phi)\rho_s]}{Dt} + (1-\phi)\rho_s \nabla \cdot \boldsymbol{v}_s = 0, \tag{8}$$

$$\frac{D^s(\phi S_\vartheta \rho_\vartheta)}{Dt} + \phi S_\vartheta \rho_\vartheta \nabla \cdot \boldsymbol{v}_s + \nabla \cdot \phi S_\vartheta \rho_\vartheta (\boldsymbol{v}_\vartheta - \boldsymbol{v}_s) = 0. \tag{9}$$

By applying the chain rule and neglecting the spatial gradient of fluid densities, Eqs. (8) and (9) can be reformulated as,

$$-\frac{D^s\phi}{Dt} + \frac{1-\phi}{\rho_s}\frac{D^s\rho_s}{Dt} + (1-\phi)\nabla \cdot \boldsymbol{v}_s = 0, \tag{10}$$

$$S_\vartheta \frac{D^s\phi}{Dt} + \phi \frac{D^s S_\vartheta}{Dt} + \frac{\phi S_\vartheta}{\rho_\vartheta}\frac{D^s\rho_\vartheta}{Dt} + \phi S_\vartheta \nabla \cdot \boldsymbol{v}_s + \nabla \cdot \phi S_\vartheta (\boldsymbol{v}_\vartheta - \boldsymbol{v}_s) = 0. \tag{11}$$

Substituting Eq. (10) into Eq. (11), one can obtain,

$$\phi\frac{D^s S_\vartheta}{Dt}+S_\vartheta\frac{1-\phi}{\rho_s}\frac{D^s\rho_s}{Dt}+\frac{\phi S_\vartheta}{\rho_\vartheta}\frac{D^s\rho_\vartheta}{Dt}+S_\vartheta\nabla\cdot\boldsymbol{v}_s+\nabla\cdot\phi S_\vartheta(\boldsymbol{v}_\vartheta-\boldsymbol{v}_s)=0. \tag{12}$$

Further substituting the EOS of each phase into Eq. (12) and expressing the derivative of S_ϑ in terms of the capillary pressure $p_c=p_g-p_l$, the equation can be reformulated as,

$$\phi\frac{\partial S_\vartheta}{\partial p_c}\frac{D^s p_c}{Dt}+\phi S_\vartheta\alpha_\vartheta\frac{D^s p_\vartheta}{Dt}-\beta_{s\vartheta}\frac{D^s T}{Dt}+S_\vartheta\nabla\cdot\boldsymbol{v}_s+\nabla\cdot\phi S_\vartheta(\boldsymbol{v}_\vartheta-\boldsymbol{v}_s)=0, \tag{13}$$

where $\beta_\vartheta=(1-\phi)S_\vartheta\beta_s+\phi S_\vartheta\beta_\vartheta$, $\frac{D^s p_c}{Dt}=\frac{D^s p_g}{Dt}-\frac{D^s p_l}{Dt}$, and $\frac{\partial S_\vartheta}{\partial p_c}=\frac{\partial S_\vartheta}{\partial p_g}=-\frac{\partial S_\vartheta}{\partial p_w}$, which can be calculated based on a given soil water retention curve. Here, the solid compressibility is futher neglected [49].

Considering $\frac{D^s S_l}{Dt}+\frac{D^s S_g}{Dt}=0$, Eq. (13) for liquid and gas can be combined into one for the mixture,

$$\phi S_l\alpha_l\frac{D^s p_l}{Dt}+\phi S_g\alpha_g\frac{D^s p_g}{Dt}-\beta_m\frac{D^s T}{Dt}+\nabla\cdot\boldsymbol{v}_s+\nabla\cdot\phi S_l(\boldsymbol{v}_l-\boldsymbol{v}_s)+\nabla\cdot\phi S_g(\boldsymbol{v}_g-\boldsymbol{v}_s)=0, \tag{14}$$

where $\beta_m=(1-\phi)\beta_s+\phi S_l\beta_l+\phi S_g\beta_g$. Note that since α_g is typically several orders larger than α_l, the compressibility of the whole system is mainly governed by α_g.

2.3.2. Momentum balance equations

For a dynamic problem in MPM, the state of motion of a fluid-infiltrated porous medium is characterized by the solid phase velocity $\boldsymbol{v}_s$ and fluid phase velocities $\boldsymbol{v}_\vartheta$ (*i.e.*, liquid velocity $\boldsymbol{v}_l$ and gas velocity $\boldsymbol{v}_g$), and is governed by independent momentum balance equation of each phase, given by [17],

$$n_\pi\rho_\pi\frac{D^s\boldsymbol{v}_\pi}{Dt}=\nabla\cdot\boldsymbol{\sigma}_\pi+n_\pi\rho_\pi\boldsymbol{b}+\boldsymbol{f}_\pi^b+\boldsymbol{f}_\pi^d, \tag{15}$$

where $\boldsymbol{\sigma}_\pi$ is the partial stress on π phase, $\boldsymbol{f}_\pi^b$ is the body force, $\boldsymbol{f}_b$ is the buoyancy force, and $\boldsymbol{f}_\pi^d$ is the drag force.

The partial stress acting on each phase is given by,

$$\boldsymbol{\sigma}_\vartheta=-\phi S_\vartheta p_\vartheta\boldsymbol{I},\quad \boldsymbol{\sigma}_s=\boldsymbol{\sigma}'-n_s p_f\boldsymbol{I}, \tag{16}$$

where p_ϑ is the pore pressure (positive in compression) of ϑ fluid, $\boldsymbol{\sigma}'$ is the effective Cauchy stress tensor (positive in tension), and $\boldsymbol{I}$ is the identity tensor. Based on the effective stress principle [53,54], the total Cauchy stress $\boldsymbol{\sigma}$ is defined by the summation of stress on each phase, which yields,

$$\boldsymbol{\sigma}=\boldsymbol{\sigma}'-p_f\boldsymbol{I},\ \text{with}\ p_f=S_l p_l+S_g p_g, \tag{17}$$

where p_f is the pore fluid pressure.

Assuming that Darcy's law is valid for fluid migration, the momentum balance equations can be formulated as,

$$\phi S_\vartheta\rho_\vartheta\frac{D^s\boldsymbol{v}_\vartheta}{Dt}=-\phi S_\vartheta\nabla p_\vartheta+\phi S_\vartheta\rho_\vartheta\boldsymbol{b}-(\phi S_\vartheta)^2\frac{\mu_\vartheta}{k_a k_{r\vartheta}}(\boldsymbol{v}_\vartheta-\boldsymbol{v}_s), \tag{18}$$

where μ_ϑ is the fluid dynamic viscosity, k_a is the absolute permeability, and $k_{r\vartheta}$ is the relative permeability, dependent on the saturation of each phase.

Since the buoyancy and drag forces are internal forces, they can be canceled if adding the momentum balance equations for all phases together, which yields the equation for the mixture,

$$(1-\phi)\rho_s\frac{D^s\boldsymbol{v}_s}{Dt}+\phi S_l\rho_l\frac{D^s\boldsymbol{v}_l}{Dt}+\phi S_g\rho_g\frac{D^s\boldsymbol{v}_g}{Dt}=\nabla\cdot\left[\boldsymbol{\sigma}'-(S_l p_l+S_g p_g)\boldsymbol{I}\right]+\rho_m\boldsymbol{b}. \tag{19}$$

2.3.3. Energy balance equation

The energy balance equation for the solid phase is formulated as,

$$(1-\phi)\rho_s c_s\frac{D^s T}{Dt}+\nabla\cdot(-\lambda_{eff,s}\nabla T)+\theta^e\boldsymbol{\eta}:\dot{\boldsymbol{\varepsilon}}^e-\theta^p\boldsymbol{\sigma}':\dot{\boldsymbol{\varepsilon}}^p=0, \tag{20}$$

where c_s and $\lambda_{eff,s}$ are respectively the specific heat capacity and the effective heat conductivity coefficient of the solid phase. The last two terms, $\theta^e\boldsymbol{\eta}:\dot{\boldsymbol{\varepsilon}}^e$ and $\theta^p\boldsymbol{\sigma}':\dot{\boldsymbol{\varepsilon}}^p$, represent respectively the thermo-elastic coupling term due to the reversible (elastic) deformation and the thermoplastic coupling term denoting the conversion of the irreversible plastic work into heat, where $\dot{\boldsymbol{\varepsilon}}^e$ and $\dot{\boldsymbol{\varepsilon}}^p$ are the elastic and plastic strain rate, $\boldsymbol{\eta}$ is the stress–temperature modulus, and θ^e and θ^p are two coefficients of heat transfer [55,56].

For the fluid phase, the convective heat transfer due to relative motion with the solid phase should be taken into consideration in the energy balance equation, given by,

$$\phi S_\vartheta\rho_\vartheta c_\vartheta\frac{D^s T}{Dt}+\phi S_\vartheta\rho_\vartheta c_\vartheta(\boldsymbol{v}_\vartheta-\boldsymbol{v}_s)\cdot\nabla T+\nabla\cdot(-\lambda_{eff,\vartheta}\nabla T)=0, \tag{21}$$

where c_ϑ and $\lambda_{eff,\vartheta}$ are respectively the specific heat capacity and the effective thermal conductivity of ϑ phase.

Since assuming identical temperature for all phases at the same material point, the energy balance equation can be written into one for the mixture,

$$C_m \frac{D^s T}{Dt} + \left(\phi S_l \rho_l c_l (\boldsymbol{v}_l - \boldsymbol{v}_s) + \phi S_g \rho_g c_g (\boldsymbol{v}_g - \boldsymbol{v}_s)\right) \cdot \nabla T + \nabla \cdot (-\lambda_m \nabla T) = Q, \tag{22}$$

where Q represents all sources of heat, C_m and λ_m are respectively the mixture heat capacity and mixture thermal conduction coefficient, given by,

$$C_m = (1-\phi)\rho_s c_s + \phi S_l \rho_l c_l + \phi S_g \rho_g c_g, \quad \lambda_m = (1-\phi)\lambda_s + \phi S_l \lambda_l + \phi S_g \lambda_g, \tag{23}$$

where λ_π is the intrinsic thermal conductivity of π phase.

2.4. Simplified balance equations for biphasic porous media

2.4.1. Homogenization of liquid–gas mixture

We do not consider the capillary pressure in the above equations such that $p_\vartheta = p_f$, and we homogenize the liquid–gas mixture as a uniform fluid phase. The collective properties of the homogenized fluid $\mathcal{P}_f$ is given by,

$$\mathcal{P}_f = S_l \mathcal{P}_l + S_g \mathcal{P}_g. \tag{24}$$

In the presented model, $\mathcal{P}_f$ can be the volume fraction, density, velocity, momentum, compressibility, thermal conductivity, specific heat capacity, permeability, and thermal conductivity. By such homogenization, the three-phase solid–liquid–gas problem can be reduced to a two-phase solid–fluid problem, as illustrated in Fig. 1.

Remark 1. Another routine to simplify the three-phase problem to a two-phase problem is assuming the gas density ρ_g and gas pressure p_g to zero. This assumption is only reasonable for porous media with dry air and water and with good gas seepage conditions. However, such simplification becomes unrealistic for two-phase gas–liquid flow with low permeability, like gas–water or gas–oil flow in energy reservoirs, where fluid compressibility plays a more significant role.

2.4.2. Reduced balance equations

The reduced form for the balance Eqs. (14), (18), (19), and (22) are summarized as follows. For brevity, the time derivative of a function f is expressed in the rate form $\dot{f}$ in the remaining content.

- *Mass balance equation of mixture*:

$$n_f \alpha_f \dot{p}_f - (n_s \beta_s + n_f \beta_f)\dot{T} + \nabla \cdot \boldsymbol{v}_s + \nabla \cdot n_f (\boldsymbol{v}_f - \boldsymbol{v}_s) = 0, \tag{25}$$

  where the fluid compressibility α_f and the fluid thermal expansivity β_f are given by,

$$\alpha_f = S_l \alpha_l + S_g \alpha_g = S_l \alpha_l + S_g / p_g, \tag{26a}$$

$$\beta_f = S_l \beta_l + S_g \beta_g = S_l \beta_l + S_g / T. \tag{26b}$$

- *Momentum balance equations of mixture and fluid phase*:

$$n_s \rho_s \dot{\boldsymbol{v}}_s + n_f \rho_f \dot{\boldsymbol{v}}_f = \nabla \cdot (\boldsymbol{\sigma}' - p_f \boldsymbol{I}) + \rho_m \boldsymbol{b}, \tag{27}$$

$$n_f \rho_f \dot{\boldsymbol{v}}_f = -n_f \nabla p_f + n_f \rho_f \boldsymbol{b} - n_f^2 \frac{\mu_f}{k_f}(\boldsymbol{v}_f - \boldsymbol{v}_s), \tag{28}$$

- *Energy balance equation of mixture*:

$$C_m \dot{T} + n_f \rho_f c_f (\boldsymbol{v}_f - \boldsymbol{v}_s) \cdot \nabla T + \nabla \cdot (-\lambda_m \nabla T) = Q, \tag{29}$$

  where $C_m = n_f \rho_f c_f + n_s \rho_s c_s$ and $\lambda_m = n_s \lambda_s + n_f \lambda_f$.

Remark 2. If α_f is small enough, then the fluid can be assumed to be incompressible, and the first term in the mass balance Eq. (25) vanishes. For isothermal conditions, the second term can further vanish. Then, the mass balance equation reduces to the well-known velocity divergence-free Poisson equation,

$$\nabla \cdot \boldsymbol{v}_s + \nabla \cdot n_f (\boldsymbol{v}_f - \boldsymbol{v}_s) = 0. \tag{30}$$

However, as indicated by the expression of α_f (Eq. (26a)), the presence of a gas phase prevents α_f from becoming negligibly small. Therefore, it should not be ignored. In practice, simulations often involve the simultaneous transition between incompressible, weakly compressible, and highly compressible fluids across both spatial and temporal scales. This requires the two-phase solver to be versatile enough to handle a wide range of pore fluid conditions.

2.4.3. Boundary conditions

Eqs. (25), (27), (28), and (29) are the primary governing equations to be solved. The THM-coupled equations are collectively subject to boundary conditions as follows.

The Dirichlet boundary conditions include the velocity, pressure, and temperature boundary conditions, given by,

$$\boldsymbol{v}_s = \hat{\boldsymbol{v}}_s \quad \text{on } \Gamma_s, \tag{31a}$$

$$\boldsymbol{v}_f = \hat{\boldsymbol{v}}_f \quad \text{on } \Gamma_f, \tag{31b}$$

$$p_f = \hat{p}_f \quad \text{on } \Gamma_p, \tag{31c}$$

$$T = \hat{T} \quad \text{on } \Gamma_T. \tag{31d}$$

The Neumann boundary conditions include the mixture traction, liquid traction, liquid flux, and heat flux boundaries, given by,

$$\boldsymbol{\sigma} \cdot \boldsymbol{n} = \hat{\boldsymbol{t}} \quad \text{on } \Gamma_t, \tag{32a}$$

$$\boldsymbol{\sigma}_f \cdot \boldsymbol{n} = \hat{\boldsymbol{t}}_f \quad \text{on } \Gamma_{tf}, \tag{32b}$$

$$-\boldsymbol{q}_f \cdot \boldsymbol{n} = \hat{q}_f \quad \text{on } \Gamma_{qf}, \tag{32c}$$

$$-\boldsymbol{q}_e \cdot \boldsymbol{n} = \hat{q}_e \quad \text{on } \Gamma_{qe}, \tag{32d}$$

where $\boldsymbol{n}$ is the outward unit normal vector.

2.4.4. Mechanical model for solid skeleton

For non-isothermal conditions, the effective stress rate is calculated by,

$$\dot{\boldsymbol{\sigma}}' = \boldsymbol{D} : \left(\dot{\boldsymbol{\varepsilon}}_s + \dot{\boldsymbol{\varepsilon}}_T\right), \tag{33}$$

where $\boldsymbol{D}$ is the tangential stiffness tensor, $\dot{\boldsymbol{\varepsilon}}_s$ and $\dot{\boldsymbol{\varepsilon}}_T$ are the mechanical strain rate and the thermal strain rate, respectively, given by,

$$\dot{\boldsymbol{\varepsilon}}_s = \frac{1}{2}\left(\nabla \boldsymbol{v}_s + (\nabla \boldsymbol{v}_s)^T\right), \quad \dot{\boldsymbol{\varepsilon}}_T = -\frac{\beta_s}{3}\dot{T}\boldsymbol{I}, \tag{34}$$

where β_s is the volumetric thermal expansivity of the solid phase, and $\dot{T}$ is the rate of temperature.

A simple elastoplastic non-associated strain-softening Mohr–Coulomb model is adopted in this study. The yield function F and the flow potential function P defined in terms of friction angle φ, cohesion c, and dilation angle ψ, are given by,

$$F = R_{mc} q + p \tan\varphi - c, \tag{35a}$$

$$P = \sqrt{(\epsilon c \tan\psi)^2 + \left(R_{mw} q\right)^2} + p \tan\psi, \tag{35b}$$

where p and q are the mean effective stress and the deviatoric stress, respectively. ϵ and e are the meridional eccentricity and the deviatoric eccentricity, respectively. In addition, R_{mc} and R_{mw} are two functions related to the Lode's angle, friction angle, and deviatoric eccentricity.

Large deformation may cause localized failure patterns in porous materials, leading to a decrease in the effective material strength with the accumulation of plastic strain. This phenomenon can be captured by a strain-softening model [21]. In this work, a simple linear strain-softening model is adopted, given as follows,

$$c = c_{peak} + \left(c_{res} - c_{peak}\right)(\varepsilon^p - \varepsilon^p_{peak})/(\varepsilon^p_{res} - \varepsilon^p_{peak}), \ \varepsilon^p \le \varepsilon^p_{peak}, \tag{36a}$$

$$\varphi = \varphi_{peak} + \left(\varphi_{res} - \varphi_{peak}\right)(\varepsilon^p - \varepsilon^p_{peak})/(\varepsilon^p_{res} - \varepsilon^p_{peak}), \ \varepsilon^p \le \varepsilon^p_{peak}, \tag{36b}$$

where ε^p is the plastic deviatoric strain and the subscripts '*peak*' and '*res*' represent the peak and residual values of strength parameters, respectively. If $\varepsilon^p > \varepsilon^p_{peak}$, $c = c_{res}$ and $\varphi = \varphi_{res}$.

3. An improved fractional step formulation in MPM

In this section, we present the weak form for the strong form equations and the MPM solution algorithms based on explicit time integration and the new semi-implicit time integration with an improved fractional step method. The optimizations of the solution algorithm aiming to improve computational efficiency and accuracy are highlighted.

3.1. Weak form and MPM discretization

By performing the standard Galerkin approximation, the weak form equivalent to the balance equations in Section 2.4.2 along with the Neumann boundary conditions can be derived as,

- *Momentum balance equations*

$$\int_\Omega \delta \boldsymbol{v}_s \cdot n_s \rho_s \dot{\boldsymbol{v}}_s dV + \int_\Omega \delta \boldsymbol{v}_s \cdot n_f \rho_f \dot{\boldsymbol{v}}_f dV = -\int_\Omega \nabla \delta \boldsymbol{v}_s : (\boldsymbol{\sigma}' - p_f \boldsymbol{I}) dV + \int_{\Gamma_t} \delta \boldsymbol{v}_s \cdot \hat{\boldsymbol{t}} dS + \int_\Omega \delta \boldsymbol{v}_s \cdot \rho_m \boldsymbol{b} dV, \tag{37}$$

$$\int_\Omega \delta \boldsymbol{v}_f \cdot n_f \rho_f \dot{\boldsymbol{v}}_f dV = -\int_\Omega \nabla \delta \boldsymbol{v}_f : (-n_f p_f \boldsymbol{I}) dV + \int_{\Gamma_{tf}} \delta \boldsymbol{v}_f \cdot \hat{\boldsymbol{t}}_f dS + \int_\Omega \delta \boldsymbol{v}_f \cdot n_f \rho_f \boldsymbol{b} dV - \int_\Omega \delta \boldsymbol{v}_f \cdot n_f^2 \frac{\mu_f}{k_f} (\boldsymbol{v}_f - \boldsymbol{v}_s) dV, \tag{38}$$

- *Energy balance equation*

$$\int_\Omega \delta T \cdot C_m \dot{T} dV + \int_\Omega \delta T \cdot n_f \rho_f c_f (\boldsymbol{v}_f - \boldsymbol{v}_s) \cdot \nabla T dV + \int_{\Gamma_{qe}} \delta T \cdot \hat{q}_e dS - \int_\Omega \delta T \cdot \nabla \cdot (-\lambda_m \nabla T) dV = \int_\Omega \delta T \cdot Q dV, \tag{39}$$

- *Mass balance equation*

$$\int_\Omega \delta p \cdot n_f \alpha_f \dot{p}_f dV - \int_\Omega \delta p \cdot (n_s \beta_s + n_f \beta_f) \dot{T} dV + \int_\Omega \delta p \cdot \nabla \cdot \boldsymbol{v}_s dV - \int_\Omega \nabla \delta p \cdot n_f (\boldsymbol{v}_f - \boldsymbol{v}_s) dV + \int_{\Gamma_{qf}} \delta p \cdot \hat{q}_f dS = 0, \tag{40}$$

where $\delta \boldsymbol{v}_s$, $\delta \boldsymbol{v}_f$, δT, and δp are arbitrary test functions with zero values on the boundaries of the corresponding fields; $\hat{\boldsymbol{t}}$, $\hat{\boldsymbol{t}}_f$, $\hat{q}_e$, and $\hat{q}_f$ are prescribed boundary mixture traction, fluid traction, heat flux, and fluid flux defined in Section 2.4.3.

The weak form equations are then discretized in space based on the generalized interpolation material point (GIMP) method [6]. Considering a material domain Ω discretized into a finite number of subdomains, each subdomain Ω_p is represented by a material point (*i.e.*, particle) located at its central position $\boldsymbol{x}_p$. For 1D condition, the interpolation function $S_{Ip} := S_I(x_p)$ and its gradient $\nabla S_{Ip} := \nabla S_I(x_p)$ regarding particle p and node I are given by,

$$S_{Ip} = \frac{1}{V_p} \int_{\Omega_p \cap \Omega} \chi_p(x) N_I(x) dV, \quad \nabla S_{Ip} = \frac{1}{V_p} \int_{\Omega_p \cap \Omega} \chi_p(x) \nabla N_I(x) dV, \tag{41}$$

where χ_p and N_I are the particle characteristic function and the grid shape function, and V_p is the particle volume. With the shape function, the physical fields and the virtual test fields can be approximated by,

$$\mathcal{V}_p = \sum_{I=1}^{N_n} S_{Ip} \mathcal{V}_I, \quad \delta \mathcal{V}_p = \sum_{I=1}^{N_n} S_{Ip} \delta \mathcal{V}_I, \tag{42}$$

where $\mathcal{V} = \boldsymbol{v}_s, \boldsymbol{v}_f, p_f, T$ represents the unknowns.

3.2. Explicit solution scheme

In explicit THM-coupled MPM, the weak form for the energy balance equation can be discretized into the following compact form,

$$\mathcal{M}_T \dot{T}^{k+1} = \mathcal{Q}^{int} + \mathcal{Q}^{ext}, \tag{43}$$

where $\mathcal{M}_T$, $\mathcal{Q}^{int}$, and $\mathcal{Q}^{ext}$ are the nodal heat capacity, internal heat, and external heat, respectively, given by,

$$(\mathcal{M}_T)_I = \sum_{p=1}^{N_p} V_p C_{mp} S_{Ip}, \tag{44a}$$

$$(\mathcal{Q}^{int})_I = -\sum_{p=1}^{N_p} V_p n_f \rho_f c_f (\boldsymbol{v}_{fp}^k - \boldsymbol{v}_{sp}^k) \nabla T_p^k S_{Ip} - \sum_{p=1}^{N_p} V_p \lambda_m \nabla T_p^k \nabla S_{Ip}, \tag{44b}$$

$$(\mathcal{Q}^{ext})_I = \sum_{p=1}^{N_p} V_p Q_p S_{Ip} - \sum_{p=1}^{N_p} V_p h_p^{-1} \hat{q}_{ep} S_{Ip}. \tag{44c}$$

where the superscripts "k" and "$k+1$" represent the current time step and the next time step, respectively, and h_p is the thickness of boundary particles.

Similarly, the momentum balance equations can be discretized as,

$$\mathcal{M}_s \dot{\boldsymbol{v}}_s^{k+1} + \mathcal{M}_f \dot{\boldsymbol{v}}_f^{k+1} = \boldsymbol{f}^{int} + \boldsymbol{f}^{ext}, \tag{45}$$

$$\mathcal{M}_f \dot{\boldsymbol{v}}_f^{k+1} = \boldsymbol{f}_f^{int} + \boldsymbol{f}_f^{ext} - \mathcal{Q}^d (\boldsymbol{v}_f^k - \boldsymbol{v}_s^k), \tag{46}$$

where $\mathcal{M}_s$ and $\mathcal{M}_f$ are the nodal mass matrices, $\mathcal{Q}^d$ is the nodal drag force coefficient, and $\boldsymbol{f}^{int}$, $\boldsymbol{f}^{ext}$, $\boldsymbol{f}_f^{int}$, and $\boldsymbol{f}_f^{ext}$ are the nodal internal and external forces, given by,

$$(\mathcal{M}_\pi)_I = \sum_{p=1}^{N_p} V_p n_{\pi p} \rho_{\pi p} S_{Ip}, \quad \pi = s, f, \tag{47a}$$

$$(\mathcal{Q}^d)_I = \sum_{p=1}^{N_p} V_p n_{fp}^2 \frac{\mu_f}{k_f} S_{Ip}, \tag{47b}$$

$$(\boldsymbol{f}^{int})_I = -\sum_{p=1}^{N_p} \nabla S_{Ip} : V_p(\boldsymbol{\sigma}_p'^k - p_{fp}^k \boldsymbol{I}), \tag{47c}$$

$$(\boldsymbol{f}^{ext})_I = \sum_{p=1}^{N_p} V_p h_p^{-1} \hat{\boldsymbol{t}}_p S_{Ip} + \sum_{p=1}^{N_p} V_p \rho_{mp} \boldsymbol{b}_p S_{Ip}, \tag{47d}$$

$$(\boldsymbol{f}_f^{int})_I = \sum_{p=1}^{N_p} V_p n_{fp} p_{fp}^k \nabla S_{Ip}, \tag{47e}$$

$$(\boldsymbol{f}_f^{ext})_I = \sum_{p=1}^{N_p} V_p h_p^{-1} \hat{\boldsymbol{t}}_{fp} S_{Ip} + \sum_{p=1}^{N_p} V_p n_{fp} \rho_{fp} \boldsymbol{b}_p S_{Ip}. \tag{47f}$$

Once the nodal variables $\dot{T}^{k+1}$, $\dot{\boldsymbol{v}}_s^{k+1}$, and $\dot{\boldsymbol{v}}_f^{k+1}$ are solved and mapped to the particles, the particle pore fluid pressure is then calculated by,

$$p_{fp}^{k+1} = p_{fp}^k + \frac{\Delta t}{n_{fp}\alpha_{fp}} \left(\beta_{mp} \dot{T}_p^{k+1} - n_{sp}^{k+1} \dot{\varepsilon}_{sp}^{k+1} - n_{fp}^{k+1} \dot{\varepsilon}_{fp}^{k+1} \right), \tag{48}$$

where Δt is the time step size, $\beta_{mp} = n_{sp}\beta_{sp} + n_{fp}\beta_{fp}$ is the mixture thermal conductivity, and $\dot{\varepsilon}_{sp} = tr(\dot{\boldsymbol{\varepsilon}}_{sp})$ and $\dot{\varepsilon}_{fp} = tr(\dot{\boldsymbol{\varepsilon}}_{fp})$ are respectively the rate of volumetric strain of the solid and fluid phases. To reduce the pressure oscillation in explicit MPM, the reduced integration is adopted for the fluid volumetric strain rate, namely, replacing $\dot{\varepsilon}_{fp}$ by the volumetric strain rate calculated at the cell center $\dot{\varepsilon}_{fc}$ [17].

3.3. Improved semi-implicit fractional step scheme

Although the explicit scheme can directly consider the fluid compressibility and is suitable for modeling dynamic problems, it has three major limitations: (1) the pressure field shows spatial oscillations even with reduced integration; (2) the time step size is dependent on the permeability and the compressibility coefficient, making it inefficient for low-permeability conditions; (3) it cannot be used to simulate incompressible limit. The semi-implicit MPM based on the fractional step method (FSM) can tackle these limitations. However, as aforementioned, the previous FSM-related MPM works are all based on the incompressible fluid assumption [19,31,34]. In this section, we introduce an improved fractional step formulation, which is applicable for both compressible and incompressible conditions and is more computationally efficient than the original FSM.

3.3.1. Semi-implicit time integration

With the semi-implicit time integration, the energy equation is still solved explicitly, whereas the mass and momentum balance equations are solved implicitly, except that the effective stress is evaluated explicitly to avoid the involution of the elastoplastic stiffness matrix. The temporally discretized mass and momentum equations are given by,

- *Mass balance equation:*

$$n_f \alpha_f \dot{p}_f^{k+1} - \beta_m \dot{T}^{k+1} + \nabla \cdot \boldsymbol{v}_s^{k+1} + \nabla \cdot n_f(\boldsymbol{v}_f^{k+1} - \boldsymbol{v}_s^{k+1}) = 0. \tag{49}$$

- *Momentum balance equations:*

$$n_s \rho_s \dot{\boldsymbol{v}}_s^{k+1} + n_f \rho_f \dot{\boldsymbol{v}}_f^{k+1} = \nabla \cdot \left(\boldsymbol{\sigma}'^k - p_f^{k+1} \boldsymbol{I} \right) + \rho_m \boldsymbol{b}, \tag{50}$$

$$n_f \rho_f \dot{\boldsymbol{v}}_f^{k+1} = -n_f \nabla p_f^{k+1} + n_f \rho_f \boldsymbol{b} - n_f^2 \frac{\mu_f}{k_f} (\boldsymbol{v}_f^{k+1} - \boldsymbol{v}_s^{k+1}). \tag{51}$$

3.3.2. Fractional step splitting

The FSM utilizes the intermediate velocities to decouple pressure and velocity fields in the momentum balance equations. Accordingly, the velocity for $\pi \in \{s, f\}$ phase can be split as,

$$\dot{\boldsymbol{v}}_\pi^{k+1} = \frac{\boldsymbol{v}_\pi^{k+1} - \boldsymbol{v}_\pi^k}{\Delta t} = \underbrace{\frac{\boldsymbol{v}_\pi^* - \boldsymbol{v}_\pi^k}{\Delta t}}_{\dot{\boldsymbol{v}}_\pi^*} + \underbrace{\frac{\boldsymbol{v}_\pi^{k+1} - \boldsymbol{v}_\pi^*}{\Delta t}}_{\dot{\boldsymbol{v}}_\pi^{**}}, \tag{52}$$

where $\boldsymbol{v}_\pi^*$ is the intermediate velocity, and $\dot{\boldsymbol{v}}_\pi^*$ and $\dot{\boldsymbol{v}}_\pi^{k+1}$ are the intermediate and corrected accelerations.

Based on Eq. (52), the momentum balance equations can be split into the predictor,

$$n_s \rho_s \dot{\boldsymbol{v}}_s^* + n_f \rho_f \dot{\boldsymbol{v}}_f^* = \nabla \cdot \left(\boldsymbol{\sigma}'^k - p_f^k \boldsymbol{I} \right) + \rho_m \boldsymbol{b}, \tag{53}$$

$$n_f\rho_f\dot{\boldsymbol{v}}_f^* = -n_f\nabla p_f^k + n_f\rho_f\boldsymbol{b} - n_f^2\frac{\mu_f}{k_f}(\boldsymbol{v}_f^* - \boldsymbol{v}_s^*), \tag{54}$$

and the corrector,

$$n_s\rho_s\dot{\boldsymbol{v}}_s^{**} + n_f\rho_f\dot{\boldsymbol{v}}_f^{**} = -\nabla(p_f^{k+1} - p_f^k), \tag{55}$$

$$n_f\rho_f\dot{\boldsymbol{v}}_f^{**} = -n_f\nabla(p_f^{k+1} - p_f^k) \underbrace{-n_f^2\frac{\mu_f}{k_f}\left(\left(\boldsymbol{v}_f^{k+1} - \boldsymbol{v}_f^*\right) - \left(\dot{\boldsymbol{v}}_s^{k+1} - \boldsymbol{v}_s^*\right)\right)}_{\text{correction for drag force}}, \tag{56}$$

where $\Delta p_f^{k+1} = p_f^{k+1} - p_f^k$ denotes the pressure increment.

Remark 3. Note that the drag force terms in the predictor are calculated using the intermediate velocities, which yields the correction term for drag force in the corrector. It was neglected in existing FSM-based two-phase MPMs [19,31,34]. However, the absence of this term would weaken the conservation of mass and momentum, thereby introducing additional errors in the velocity fields and causing over-dissipation of pore pressure. In this work, we reconsider the correction term to enhance the accuracy.

Eqs. (55) and (56) can be reformulated as,

$$n_s\rho_s\dot{\boldsymbol{v}}_s^{**} = -\xi_s n_s\nabla(p_f^{k+1} - p_f^k), \tag{57}$$

$$n_f\rho_f\dot{\boldsymbol{v}}_f^{**} = -\xi_f n_f\nabla(p_f^{k+1} - p_f^k), \tag{58}$$

where ξ_s and ξ_f are given by,

$$\xi_l = \frac{1 + \Delta t n_f^2\frac{\mu_f}{k_f}\frac{1}{n_f n_s\rho_s}}{1 + \Delta t n_f^2\frac{\mu_f}{k_f}\left(\frac{1}{n_f\rho_f} + \frac{1}{n_s\rho_s}\right)}, \quad \xi_s = \frac{1 + \Delta t n_f^2\frac{\mu_f}{k_f}\frac{1}{n_s n_f\rho_f}}{1 + \Delta t n_f^2\frac{\mu_f}{k_f}\left(\frac{1}{n_f\rho_f} + \frac{1}{n_s\rho_s}\right)}. \tag{59}$$

By substituting Eqs. (57) and (58) into Eq. (49), the mass balance equation can be reformulated into the pressure Poisson equation,

$$\Delta t\left(\xi_s\frac{n_s}{\rho_s} + \xi_f\frac{n_f}{\rho_f}\right)\nabla^2(p_f^{k+1} - p_f^k) - n_f\alpha_f\dot{p}_f^{k+1} + \beta_m\dot{T}^{k+1} - \nabla\cdot\boldsymbol{v}_s^* - \nabla\cdot n_f(\boldsymbol{v}_f^* - \boldsymbol{v}_s^*) = 0. \tag{60}$$

The modification to consider drag force correction is simply by multiplying two scalar coefficients on the pressure gradient. Therefore, the original solution scheme for FSM still holds: first, the rate of temperature is solved explicitly, and the intermediate accelerations are then solved based on Eqs. (53) and (54), and then the incremental pore pressure is solved from Eq. (60), and finally the accelerations are corrected based on Eqs (57) and (58).

3.3.3. Discretized form

Since the energy balance equation is still solved explicitly, its discretized form is nothing different from that shown in Section 3.2. The split momentum and mass balance equations based on the FSM can be further discretized as follows.

- Predictor to solve the intermediate accelerations $\dot{\boldsymbol{v}}_s^*$ and $\dot{\boldsymbol{v}}_f^*$:

$$\begin{bmatrix}\mathcal{M}_s & \mathcal{M}_f\\ -\Delta t\mathcal{Q}^d & \mathcal{M}_f + \Delta t\mathcal{Q}^d\end{bmatrix}\begin{Bmatrix}\dot{\boldsymbol{v}}_s^*\\ \dot{\boldsymbol{v}}_f^*\end{Bmatrix} = \begin{Bmatrix}\boldsymbol{f}^{int} + \boldsymbol{f}^{ext}\\ \boldsymbol{f}_f^{int} + \boldsymbol{f}_f^{ext} - \mathcal{Q}^d(\boldsymbol{v}_f^k - \boldsymbol{v}_s^k)\end{Bmatrix}. \tag{61}$$

- Pressure Poisson equation to solve incremental pore pressure $\Delta p_f^{k+1} = p_f^{k+1} - p_f^k$:

$$\left[\mathcal{L}_f + \mathcal{K}_f\right]\left\{\Delta p_f^{k+1}\right\} = \left\{\mathcal{F}_T\dot{T}^{k+1} + \boldsymbol{\mathcal{F}}_s\cdot\boldsymbol{v}_s^* + \boldsymbol{\mathcal{F}}_f\cdot(\boldsymbol{v}_f^* - \boldsymbol{v}_s^*)\right\}. \tag{62}$$

- Corrector to solve corrected accelerations $\dot{\boldsymbol{v}}_s^{k+1}$ and $\dot{\boldsymbol{v}}_f^{k+1}$:

$$\begin{bmatrix}\mathcal{M}_s & 0\\ 0 & \mathcal{M}_f\end{bmatrix}\begin{Bmatrix}\dot{\boldsymbol{v}}_s^{k+1}\\ \dot{\boldsymbol{v}}_f^{k+1}\end{Bmatrix} = \begin{Bmatrix}\boldsymbol{\mathcal{N}}_s\Delta p_f^{k+1} + \mathcal{M}_s\dot{\boldsymbol{v}}_s^*\\ \boldsymbol{\mathcal{N}}_f\Delta p_f^{k+1} + \mathcal{M}_f\dot{\boldsymbol{v}}_f^*\end{Bmatrix}. \tag{63}$$

The components of the above nodal matrices and force vectors, $\mathcal{M}_s$, $\mathcal{M}_f$, $\mathcal{Q}^d$, $\boldsymbol{f}^{int}$, $\boldsymbol{f}^{ext}$, $\boldsymbol{f}_f^{int}$, and $\boldsymbol{f}_f^{ext}$, are the same as those in the explicit scheme, if lumped matrices are employed. The components of the additional matrices $\mathcal{L}_p$, $\mathcal{M}_p$, $\mathcal{F}_T$, $\boldsymbol{\mathcal{F}}_s$, $\boldsymbol{\mathcal{F}}_f$, $\boldsymbol{\mathcal{N}}_s$, and $\boldsymbol{\mathcal{N}}_f$ are given by,

$$(\mathcal{L}_f)_{IJ} = \sum_{p=1}^{N_p} V_p\Delta t\left(\xi_{sp}\frac{n_{sp}}{\rho_{sp}} + \xi_{fp}\frac{n_{fp}}{\rho_{fp}}\right)\nabla S_{Ip}\nabla S_{Jp}, \tag{64a}$$

$$(\mathcal{K}_f)_{IJ} = \sum_{p=1}^{N_p} V_p\Delta t^{-1}n_{fp}\alpha_{fp}S_{Ip}S_{Jp}, \tag{64b}$$

$$(\mathcal{F}_T)_{IJ} = \sum_{p=1}^{N_p} V_p \beta_{mp} S_{Ip} S_{Jp}, \tag{64c}$$

$$(\boldsymbol{\mathcal{F}}_s)_{IJ} = -\sum_{p=1}^{N_p} V_p S_{Ip} \nabla S_{Jp}, \tag{64d}$$

$$(\boldsymbol{\mathcal{F}}_f)_{IJ} = \sum_{p=1}^{N_p} V_p n_{fp} \nabla S_{Ip} S_{Jp}, \tag{64e}$$

$$(\boldsymbol{\mathcal{N}}_\pi)_{IJ} = -\sum_{p=1}^{N_p} V_p \xi_{\pi p} n_{\pi p} S_{Ip} \nabla S_{Jp}, \ \pi = s, f. \tag{64f}$$

Remark 4. Eqs. (61) and (62) represent two implicit, computationally intensive steps in each solution loop due to large matrix assemblies and iterative solvers. Between them, Eq. (61) is notably more demanding, as it involves solving for multiple-directional degrees of freedom and two field variables. To mitigate this cost, we adopt lumped matrices for $\mathcal{M}_s$, $\mathcal{M}_f$, and $\mathcal{Q}^d$, enabling a node-wise implicit scheme that decouples the system into node-level solves for intermediate accelerations, *i.e.*,

$$\begin{bmatrix} \mathcal{M}_s & \mathcal{M}_f \\ -\Delta t \mathcal{Q}^d & \mathcal{M}_f + \Delta t \mathcal{Q}^d \end{bmatrix}_I \begin{Bmatrix} \dot{\boldsymbol{v}}_s^* \\ \dot{\boldsymbol{v}}_f^* \end{Bmatrix}_I = \begin{Bmatrix} \boldsymbol{f}^{int} + \boldsymbol{f}^{ext} \\ \boldsymbol{f}_f^{int} + \boldsymbol{f}_f^{ext} - \mathcal{Q}^d(\boldsymbol{v}_f^k - \boldsymbol{v}_s^k) \end{Bmatrix}_I. \tag{65}$$

This approach helps to (1) significantly improve the computational efficiency by eliminating iterative solvers while retaining stability; (2) maintain time-step flexibility, as the critical time step remains independent of permeability, and (3) preserve accuracy, as demonstrated in case studies. Compared to Yuan et al. [34]'s explicit method for solving momentum predictors, this implicit method differs in approximating the drag force using $(\dot{\boldsymbol{v}}_f^* - \dot{\boldsymbol{v}}_s^*)$ instead of $(\dot{\boldsymbol{v}}_f^* - \dot{\boldsymbol{v}}_s^k)$. This choice helps gain the same efficiency as their explicit method while avoiding introducing additional errors for the solid velocity update in high-frequency dynamic and large deformation problems.

3.3.4. Completed solution algorithm

The solution procedure for the proposed new two-phase MPM with enhanced FSM is briefly given as follows:

Step 1: At the beginning of each time step, initialize the background mesh and compute the shape functions based on the relative location of particles in each element.

Step 2: Map the particle velocities and temperature to nodes and compute the particle strains, stresses, porosity, densities, and volumes.

Step 3: Assemble nodal coefficient matrices and force vectors based on particle properties. Note that the lumped matrices are adopted for $\mathcal{M}_T$, $\mathcal{M}_s$, $\mathcal{M}_f$, and $\mathcal{Q}^d$ in this study.

Step 4: Compute updated nodal temperature rate $\dot{T}^{k+1}$ by solving Eq. (43), and compute the intermediate accelerations $\dot{\boldsymbol{v}}_s^*$ and $\dot{\boldsymbol{v}}_f^*$ by solving Eq. (65).

Step 5: Compute updated pore pressure increment, Δp_f^{k+1}, based on updated $\dot{T}^{k+1}$ and intermediate velocities, $\boldsymbol{v}_s^*$ and $\boldsymbol{v}_f^*$, by solving Eq. (62).

Step 6: Compute the corrected acceleration, $\dot{\boldsymbol{v}}_s^{k+1}$ and $\dot{\boldsymbol{v}}_f^{k+1}$, and the end-of-step velocities, $\boldsymbol{v}_s^{k+1}$ and $\boldsymbol{v}_f^{k+1}$, based on the updated Δp_f^{k+1} by solving Eq. (78).

Step 7: Map the updated nodal temperature rate, accelerations, and pore pressure increment to particles, and update the particle temperature, velocities, displacements, and coordinates.

Step 8: If the current time $t < t_f$, go to the next loop; otherwise, terminate the simulation.

In summary, the improved fractional step formulation introduces three key advancements over the original framework [19,31]:

- **Compressible fluid compatibility**: Inclusion of the compressibility term $n_f \alpha_f \dot{p}_f^{k+1}$ in the pressure Poisson equation enables the modeling of compressible fluids and offers a critical extension for scenarios like unsaturated soils or thermo-hydro-mechanical systems.
- **Enhanced accuracy via drag force correction**: Introduction of correction coefficients ξ_s and ξ_f in the momentum corrector and pressure Poisson equation helps to refine drag force coupling and improve accuracy for dynamic, large deformation problems.
- **Efficient node-based implicit algorithm**: A novel node-wise implicit scheme for solving intermediate accelerations helps to significantly improve the computational efficiency in each time step while preserving numerical stability and accuracy.

4. Numerical examples

This section presents a series of 1D and 2D hydro-mechanical (Section 4.1) and thermo-hydro-mechanical (Section 4.2) coupling examples to show the performance of the new FSM-based MPM in simulating porous media with compressible fluid. The last

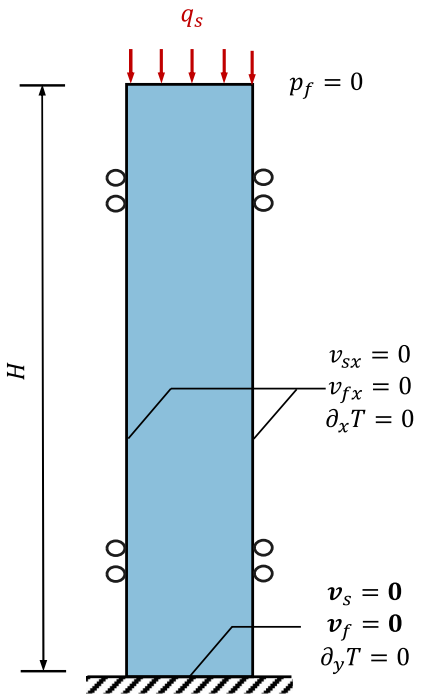

Fig. 2. Geometry and boundary conditions of 1D consolidation problem.

example further demonstrates the efficacy of the proposed approach in simulating large deformations in porous media with different fluid compressibilities. For comparison, we also present the results based on the explicit sequential solution scheme presented in Section 3.2. For brevity, in the following analysis, the semi-implicit FSM is simply denoted as the "FSM" scheme, while the explicit sequential scheme is denoted as the "explicit" scheme.

4.1. Hydro-mechanical coupling problems

4.1.1. 1D wave propagation

The first example examines the propagation of a pressure wave, a phenomenon of wave shock within a saturated soil column, which is a common dynamic feature of compressible fluid in porous media [3,16]. The geometry and boundary conditions of the problem are shown in Fig. 2. The height and width of the soil column are set as $H = 2.5$ m and $L = 0.0025$ m, respectively. To accurately capture the wavefront dynamics, the domain is discretized using a highly refined mesh with 1,000 uniform quadrilateral cells and 4,000 particles. The bottom of the soil is fully fixed, whereas the left and right sides are only fixed in the normal direction. The top is a free surface and drained boundary, *i.e.*, a zero-pressure boundary, while other boundaries are impermeable. A surface surcharge of $q_s = 1$ kPa is prescribed on the top surface instantaneously at the beginning of the simulation. The initial pressure and stresses are set as zero, and the gravitational force is not considered in this example. The soil is modeled as a linear elastic material. The material properties are given as follows: solid grain density $\rho_s = 2{,}650$ kg/m^3, fluid density $\rho_f = 1{,}000$ kg/m^3, porosity $\phi = 0.4$, Young's modulus $E = 5{,}000$ MPa, Poisson's ratio $\nu = 0$, fluid viscosity $\mu_f = 1\times10^{-3}$ Pa s, and fluid compressibility $\alpha_f = 0.5\times10^{-9}$ Pa^{-1}. Two different permeabilities are considered: $k_f = 1\times10^{-12}$ m^2 and $k_f = 1\times10^{-10}$ m^2. A time step size $\Delta t = 1\times10^{-6}$ s is adopted for both the FSM and Explicit schemes.

The theoretical solution for the initial pore pressure and effective stress after the instantaneous loading was given by Verruijt [47],

$$p_0 = \frac{1/M}{\phi/K_f + 1/M}\sigma, \tag{66}$$

$$\sigma_0' = \frac{\phi/K_f}{\phi/K_f + 1/M}\sigma, \tag{67}$$

where M is the P-wave modulus, K_f is the liquid bulk modulus, and σ is the total stress equaling the applied surface traction. For this case with $M = 5{,}000$ MPa and $K_f = 1/\alpha_f = 2{,}000$ MPa, the applied surface traction will be carried out equally by the fluid and solid phases at first, that is, $p_0 = \sigma_0' = 0.5$ kPa. According to Biot's consolidation theory for saturated porous media with compressible fluid [47,54], there are normally two waves generated in the porous media due to the instantaneous application of surface loading. The first wave is known as the undrained wave, where the fluid and solid move synchronously at the same speed.

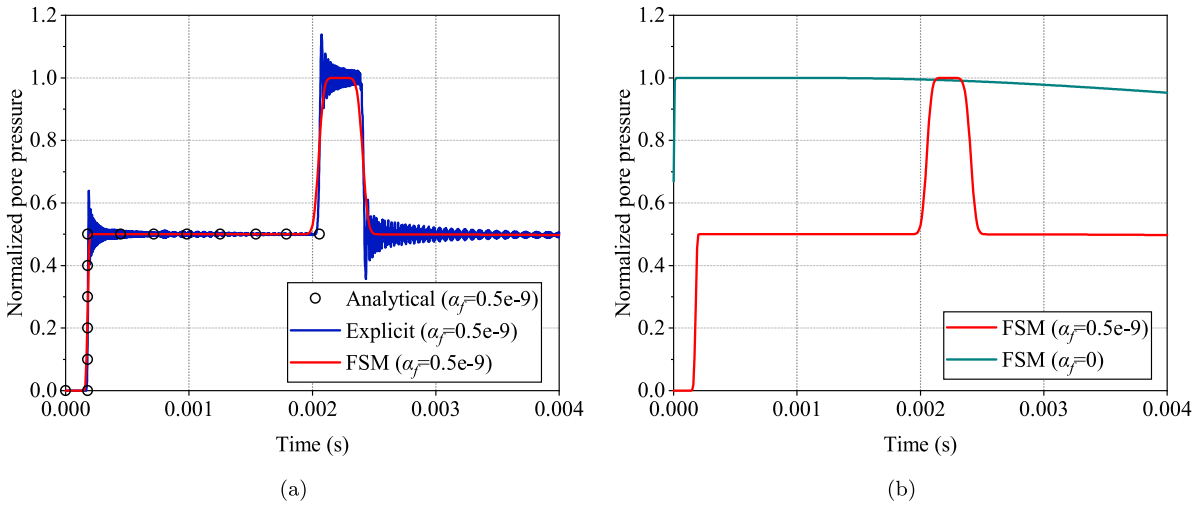

Fig. 3. Normalized pore pressure versus time at the depth of 0.4 m for the high permeability case ($k_f = 1\times10^{-10}$ m^2): (a) comparison of results by FSM, explicit scheme, and analytical solution; (b) comparison of FSM results with and without considering fluid compressibility.

The second wave is called the damped wave, where the fluid and the solid move asynchronously. The propagation speed of these two waves is given by,

$$c_u = \sqrt{\frac{M + K_f/\phi}{\rho_m}}, \tag{68}$$

$$c_d = \sqrt{\frac{\phi M}{(1-\phi)K_f + \phi M}}\sqrt{\frac{K_f}{\rho_f}}. \tag{69}$$

For the given problem, the two speeds are calculated as c_u = 2,236 m/s and c_d = 1,118 m/s.

Fig. 3(a) shows the normalized pressure versus time at a depth of 0.4 m for the case with low permeability. In this case, only the undrained wave is visible due to low-speed relative motion between the fluid and solid phases. The undrained wave arrives at a depth of 0.4 m at a time of about 1.8×10^{-4} s, which agrees well with the theoretical solution. The observed peak pressure and effective stress in the column are both 0.5 kPa, which are in good agreement with the theoretical solution. The wave arrives at the bottom after about 1.1×10^{-3} s and then is reflected back with doubled amplitude due to the rigid boundary condition at the bottom. The reflected wave arrives at a depth of 0.4 m at a time approximately 2×10^{-3} s, which is also consistent with the calculated time based on the undrained wave speed. For the high permeability case, as shown in Fig. 4(a), the undrained wave arrives at a depth of 0.4 m at a time of 1.8×10^{-4} s, which is consistent with the high permeability case, whereas the arrival time for the damped wave is around 3.6×10^{-4} s since the damped wave only has half the speed of the undrained wave. After the arrival of the damped wave, the pore pressure decreased sharply to approximately 0.3 kPa due to the strong interaction between the solid and fluid phases. For the high permeability case, the fluid and the solid move with large relative velocities, and thus, the damped wave is strongly damped out due to the interaction between the two phases. Figs. 3(a) and 4(a) show that MPM with the compressible FSM scheme can capture the correct wave propagation as that with the explicit scheme. Moreover, pressure oscillations are observed in the simulation results with the explicit scheme, which is also observed in previous explicit SPFEM [3] and MPM work [16,57]. In contrast, the results based on FSM show almost no pressure oscillations, indicating that it can filter the numerical noises and stabilize the simulation results. However, for FSM with $\alpha_f = 0$, as shown in Figs. 3(b) and 4(b), the time-dependent pressure term is absent so that the dynamic wave propagation cannot be captured.

4.1.2. 1D consolidation

In Terzaghi's 1D consolidation theory, the pore fluid and the solid grains are assumed to be incompressible. In the later development of the theory, compression of the pore fluid and particles has been taken into account [54]. In this example, the 1D consolidation tests with different fluid compressibilities are conducted. The geometry and boundary conditions are basically the same as the previous 1D wave propagation example (see Fig. 2) except that the height and the width of the soil column are set as H = 1.0 m and L = 0.02 m, respectively, and the surface surcharge is set as q_s = 10 kPa. The computational domain is discretized into 50 uniform quadrilateral cells and 200 particles. Since a clear wavefront is no longer the primary concern of this example, a relatively coarse mesh is adopted. Again, no gravitational force is considered. The soil is modeled as a linear elastic material, with material parameters given as follows: ρ_s = 2,650 kg/m^3, ρ_f = 1,000 kg/m^3, ϕ = 0.4, $\alpha_f = 0.5\times10^{-9}$ Pa^{-1}, E = 10 MPa, ν = 0.0, $\mu_f = 1\times10^{-3}$ Pa s, and $k_f = 1\times10^{-10}$ m^2. The Terzaghi's 1D consolidation solutions for pore fluid pressure p_f at the depth x and

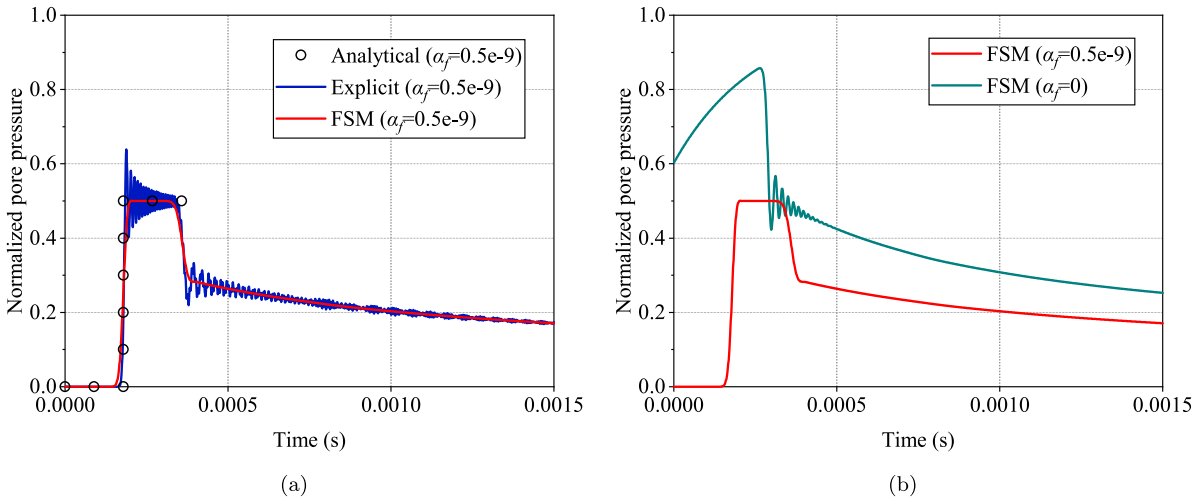

Fig. 4. Normalized pore pressure versus time at the depth of 0.4 m for the low permeability case ($k_f = 1 \times 10^{-12}$ m^2): (a) comparison of results by FSM, explicit scheme, and analytical solution; (b) comparison of FSM results with and without considering fluid compressibility.

Table 1
Comparison of the elapsed CPU time for different tests simulated by the original FSM and the improved FSM with node-wise implicit scheme.

Test	N_p	N_n	Δt	N_{steps}	Original-	Improved-	Time saved
Section 4.1.2	200	102	2.5×10^{-4}	40,000	44.1 s	34.7 s	21.3%
Section 4.1.3	26,800	6,885	5×10^{-4}	4,000	530.3 s	322.2 s	39.2%
Section 4.2.1	200	102	2.5×10^{-4}	40,000	50.9 s	39.7 s	22.0%
Section 4.2.2	25,600	6,561	1×10^{-4}	10,000	1,316.8 s	877.2 s	33.4%

time t and for the surface displacement u_s are given as follows,

$$p_f(x,t) = q_s \sum_{n=0}^{\infty} \frac{2}{\xi H} \sin(\xi x) e^{-\xi^2 ct}, \tag{70a}$$

$$u_s(t) = -\frac{q_s}{M} + \frac{q_s}{M} \sum_{n=0}^{\infty} \frac{2}{\xi^2 H} e^{-\xi^2 ct}, \tag{70b}$$

where $\xi = (2n+1)\pi/(2H)$, H is the height of the soil column, q_s is the surface surcharge, M is the P-wave modulus, and $c = k_f M/(\rho_f g)$ is the consolidation coefficient.

We first assess the numerical accuracy of the improved FSM with drag-force correction (DC) and node-wise implicit (NI) scheme. The accuracy is quantified using the relative error, e_r, defined as,

$$e_r = \sqrt{\frac{1}{N_p} \sum_{p=1}^{N_p} (p_{f,\mathrm{MPM}} - p_{f,\mathrm{ANA}})^2}, \tag{71}$$

where $p_{f,\mathrm{MPM}}$ and $p_{f,\mathrm{ANA}}$ denote pore pressures from MPM simulations and analytical solution, respectively, and N_p is the total number of particles. Four permeability values spanning from 1×10^{-10} m^2 to 1×10^{-13} m^2 were tested. At dimensionless time $T_v = ct/H^2 = 0.1$, Fig. 5(a) demonstrates a 50% reduction in e_r with DC, highlighting its role in enhancing accuracy. Moreover, the NI Scheme maintains comparable accuracy while reducing computational time by 20%–30%, as illustrated in Fig. 5(b). To generalize these findings, we evaluated CPU times for larger-scale 2D wave propagation (Section 4.1.3) and thermo-poroelastic problems (Section 4.2.2), as summarized in Table 1. Simulations were conducted on an Intel 32-Core i9-13980HX CPU with OpenMP parallelization. The efficiency gains from the NI scheme become more pronounced as particle count increases, as the original FSM's matrix assembly and iterative momentum predictor solutions scale poorly with problem size. By contrast, the improved FSM minimizes these bottlenecks, achieving superior scalability for high-resolution models.

We further evaluated the performance of the compressible FSM. Given the lack of analytical solutions for dynamic two-phase systems with compressible fluids, we validated the MPM results against explicit FEM simulations generated by a custom python-based solver. As shown in Fig. 6(a), the pore pressure profiles at the base of the soil column exhibit nearly identical fluctuations between the FSM, explicit MPM, and FEM results when using a fixed time step size $\Delta t = 1 \times 10^{-5}$ s. This alignment confirms the accuracy of the compressible FSM in resolving transient pressure waves under dynamic, compressible condition. The fluctuations represent physical pressure waves within porous media induced by instantaneous loading, as per prior analyses. Similarly, the theoretical value of initial pore pressure can be calculated, which is about 9.98 kPa, equal to the applied surface traction approximately. The

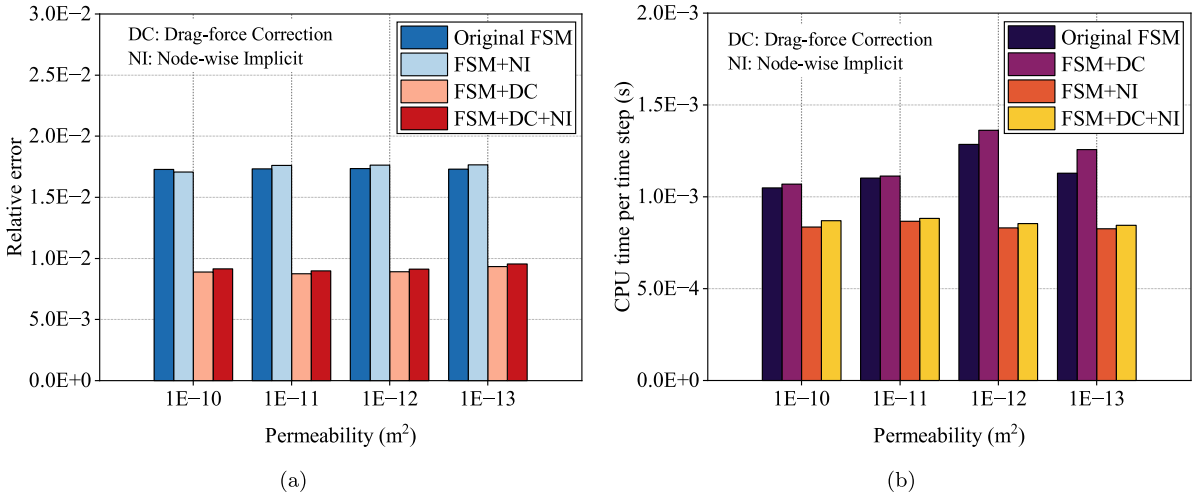

Fig. 5. Comparison of (a) numerical accuracy and (b) computational cost for the original FSM and the improved FSM.

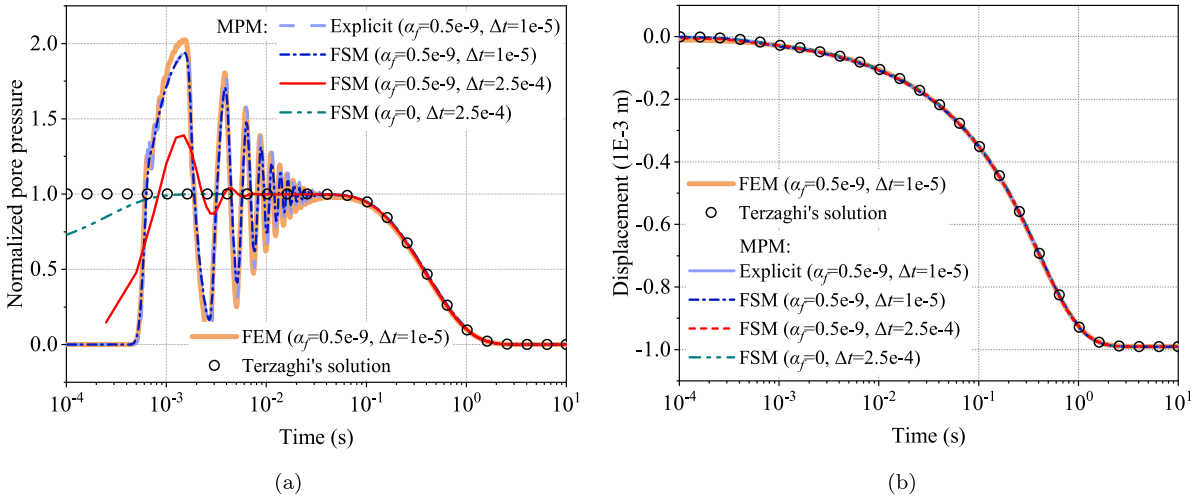

Fig. 6. Evolution of (a) pore pressure at the bottom of the soil column and (b) the surface displacement.

undrained wave speed is calculated at about 1,587 m/s, and accordingly, the undrained wave arrives at the bottom of the soil at about 4.5×10^{-4} s. As depicted in Fig. 6(a), the first pressure shock occurs at about 4.5×10^{-4} s and the peak is nearly twice the applied surface traction, which is consistent with theoretical values. The wave dissipates very rapidly, vanishing after several wave periods. However, if fluid compressibility is not considered, such pressure waves cannot be captured. Since the FSM can set a larger time step size, we also test the case with $\Delta t = 2.5 \times 10^{-4}$ s, 25 times larger than the previous one. It is observed that a large time increment can accelerate the damping of pressure waves. Once the pressure wave is completely attenuated, pressure dissipation curves for all tests converge to a nearly uniform one, consistent with Terzaghi's analytical solution. Fig. 6(b) further displays the simulated displacements for all cases. No obvious oscillation is observed from the consolidation curve, and they all align well with Terzaghi's analytical solution.

We further tested three additional cases with higher fluid compressibility values, *i.e.*, 1×10^{-8}, 1×10^{-7}, and 1×10^{-6} Pa^{-1}. Fig. 7(a) shows the bottom pore pressure and the surface displacement. The FEM results and the explicit MPM results are also shown for comparison. The conclusion is basically the same as the former case. If using the same time step size, the FSM scheme can give nearly identical pressure wave propagation and dissipation features as the explicit MPM and FEM results for all three cases. However, with a larger time step size, the pressure waves simulated by the FSM are quickly damped, similar to that observed in Fig. 6(a). It is also evident that the amplitude of the pressure wave decreases with α_f, while the length of the pressure wave increases with α_f. Again, the simulated peak values for pore pressure are consistent with the calculated value by Eq. (66), *i.e.*, 19.2, 14.3, and 4.0 kPa for $\alpha_f = 1 \times 10^{-8}$, 1×10^{-7}, and 1×10^{-6} Pa^{-1}, respectively. And, the time when the wave propagates to the bottom is also consistent with the calculated value based on Eq. (68), *i.e.*, 2.77×10^{-3}, 7.54×10^{-3}, and 1.26×10^{-2} s for $\alpha_f = 1 \times 10^{-8}$, 1×10^{-7},

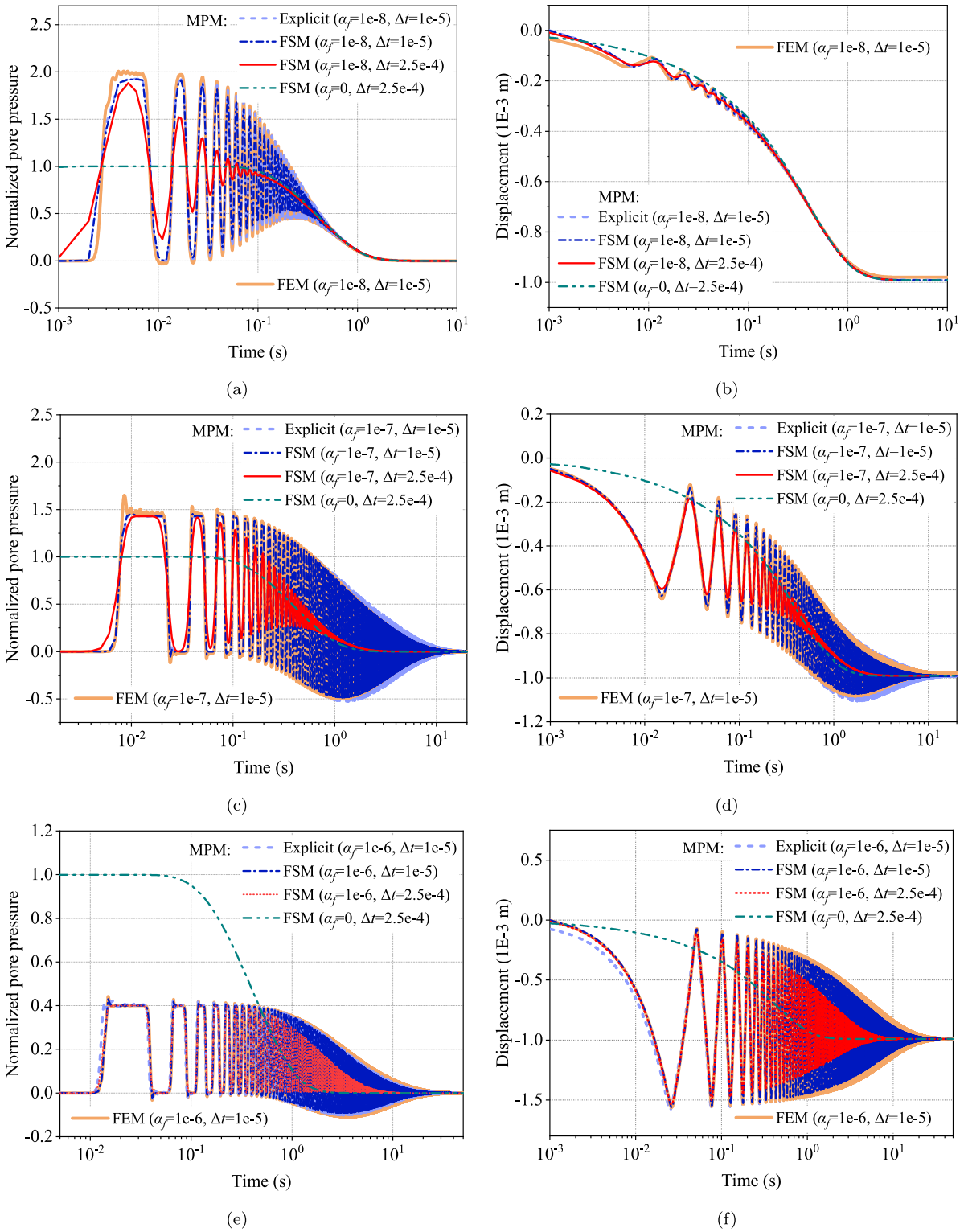

Fig. 7. Evolution of pore pressure at the bottom of the soil column and the surface displacement for (a–b) $\alpha_f = 1\times10^{-8}$ Pa^{-1}, (c–d) $\alpha_f = 1\times10^{-7}$ Pa^{-1}, and (e–f) $\alpha_f = 1\times10^{-6}$ Pa^{-1}.

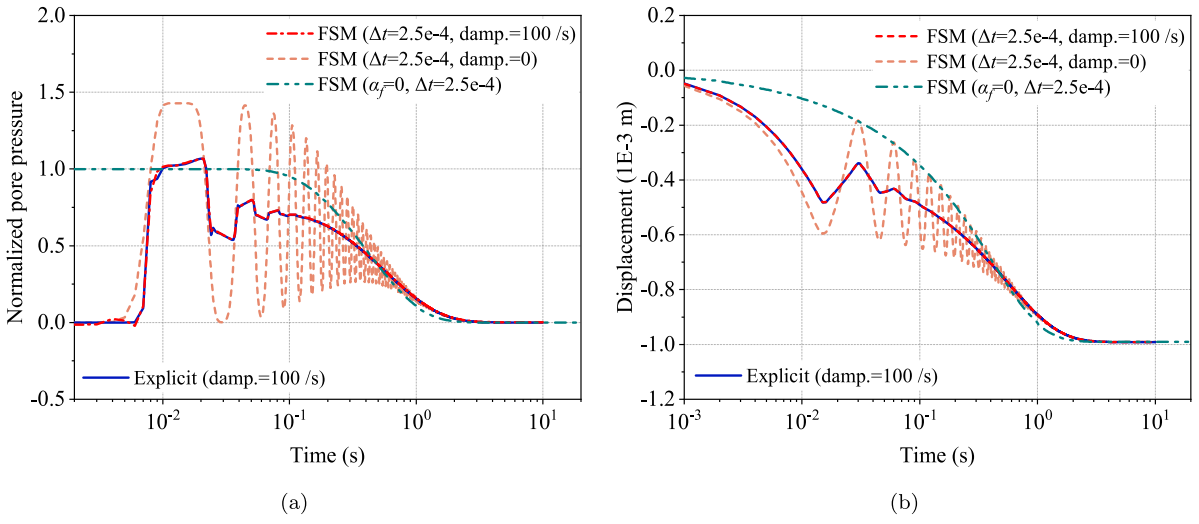

Fig. 8. Effect of particle damping on vanishing the oscillation of (a) pore pressure at the bottom of the soil column and (b) the surface displacement, taking $\alpha_f = 1 \times 10^{-7}$ Pa^{-1} as an example.

and 1×10^{-6} Pa^{-1}, respectively. However, the displacement fields show more oscillations than the low compressibility case. The amplitude seems to increase with growing α_f, with their frequency keeping in tune with the pore pressure wave. It is worth noting that with increasing α_f, the pressure responses significantly deviate from Terzaghi's solution derived based on the incompressible fluid assumption.

The simulation results indicate that although the semi-implicit FSM scheme was originally designed for incompressible fluid, it can be effectively employed in simulating porous media with compressible fluid, albeit with a compromise on certain dynamic effects when using larger time step sizes. Nevertheless, there are instances where these dynamic effects are undesirable. One way to stabilize the pressure is by introducing artificial damping to particle accelerations. Fig. 8 indicates that particle damping can effectively help to reduce oscillations [23]. However, a proper damping ratio is important for the success of the stabilization of pressure. Based on our experience, it is advised that the damping ratio should not surpass the undrained wave speed. Otherwise, over-dissipation will be observed. A more physical approach to dismissing the wave reflection is to prescribe the absorbing boundary for an artificially fixed boundary; see for Refs. [16,58].

4.1.3. 2D wave propagation

This example simulates the dynamic wave propagation in a saturated porous medium, which has been well benchmarked to validate FEM codes [3,39]. A rectangular domain with a height of 10 m and a width of 21 m is simulated. The bottom of the domain is fixed while the left and right sides are roller boundaries. The top surface is free and drained, whereas the other boundaries are impermeable. An impulse surface surcharge of $q = f(t)$ with a width of 1 m is applied on the middle of the top surface. The impulse loading is given as $f(t) = 10^5 \sin(25\pi t)$ before 0.04 s, after which the surcharge is removed. Due to symmetry, only half of the domain is simulated. The geometry, boundary conditions, and loading function are depicted in Fig. 9. The half domain is discretized into 6,720 uniform quadrilateral cells and 26,880 particles. The porous medium is modeled as a linear elastic material. The material properties are given as follows: $\rho_s = 2{,}000$ kg/m^3, $\rho_f = 1{,}000$ kg/m^3, $\phi = 0.33$, $\alpha_f = 0.5 \times 10^{-9}$ Pa^{-1}, $E = 14.5$ MPa, $\nu = 0.3$, $\mu_f = 1 \times 10^{-3}$ Pa s, and $k_f = 1 \times 10^{-9}$ m^2. The gravitational force is not considered. From previous 1D examples, it is found that the temporal resolution may have a great influence on the pressure responses using the FSM scheme. In this 2D case, the effect of time step size is also investigated. For the explicit scheme, a smaller time step size $\Delta t = 1 \times 10^{-5}$ s is adopted, while for the fractional step scheme, both a larger time step size $\Delta t = 2.5 \times 10^{-4}$ s and a smaller one $\Delta t = 1 \times 10^{-5}$ s are tested.

Fig. 10(a) plots the pore pressure evolution at point A before 0.2 s. Pressure oscillations are observed after 0.04 s, the time after the impulse loading, for both FSM and explicit schemes with $\alpha_f = 0.5 \times 10^{-9}$ Pa^{-1}. Notably, if using the same $\Delta t = 1 \times 10^{-5}$ s, the FSM can capture almost identical oscillations as the explicit scheme. With a larger $\Delta t = 5 \times 10^{-4}$ s, the oscillations become less significant but still visible. By contrast, without considering the fluid compressibility ($\alpha_f = 0$), the FSM yields a rather smooth pressure. These observations are consistent with the 1D cases. Generally, the MPM results agree well with the FEM results by Markert et al. [39] and SPFEM results by Yuan et al. [3]. Notably, the MPM results based on the incompressible FSM formulation match quite well with the SPFEM results. Yuan et al. [3] also compared the explicit and FSM schemes with compressible fluids, but no pressure fluctuation after 0.04 s was observed in their results. One possible reason is that the SPFEM algorithm over-smoothed the pressure. Fig. 10(b) further shows the movement of the material point at a surface Point B. The trajectory of point B shows an elliptic particle movement, a typical Rayleigh wave-specific motion. The numerical results obtained by different MPM schemes are nearly identical. Again, the coupled MPM results match rather well with the results in the literature. The contours of pore pressure at the time instances of

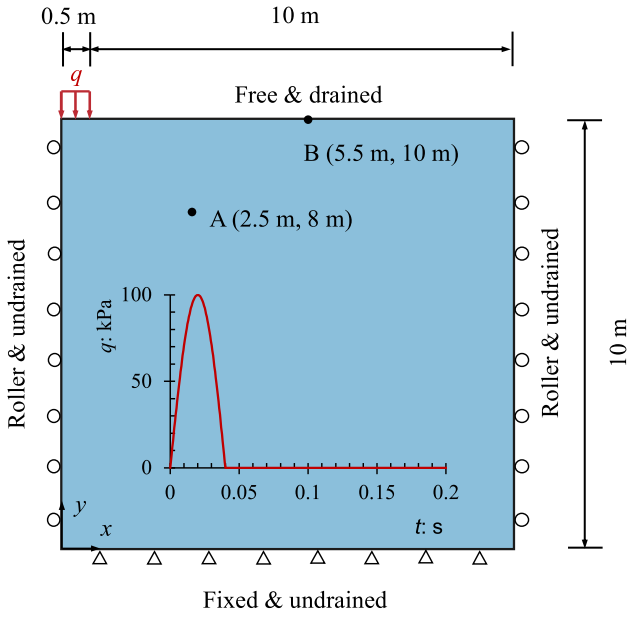

Fig. 9. Geometry, boundary conditions, and loading function of the 2D wave propagation problem.

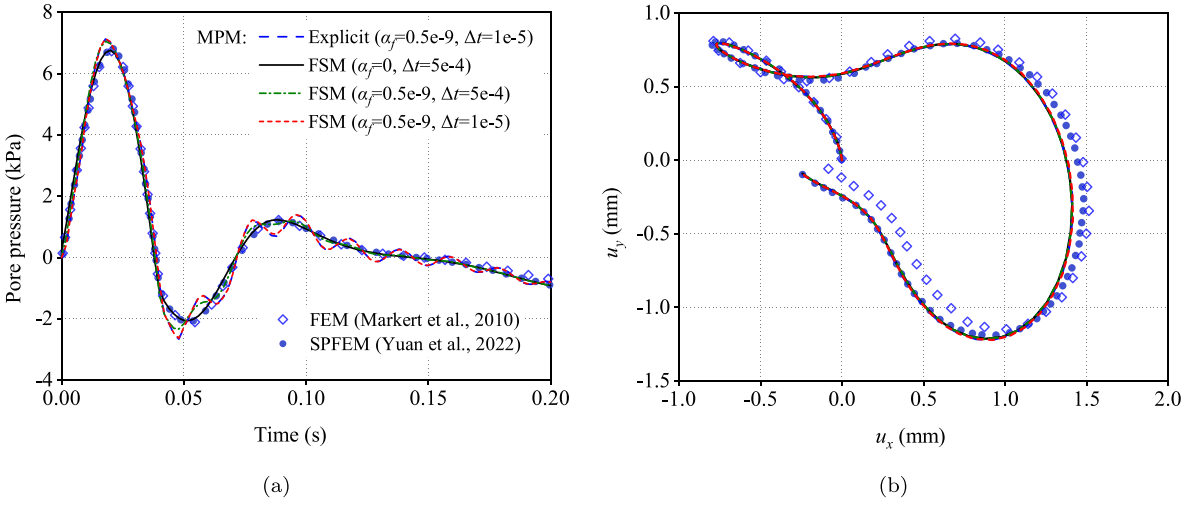

Fig. 10. (a) Pore pressure evolution at point A and (b) particle trajectory at point B.

0.1 s and 0.2 s are presented in Fig. 11. The pressure distributions are basically the same for all four tests. Minor differences are observed between the FSM with $\Delta t = 5 \times 10^{-4}$ s and the explicit scheme. However, the gaps become invisible given the same Δt.

We further tested cases with large fluid compressibility, for example, $\alpha_f = 1 \times 10^{-6}$ Pa^{-1}. Due to the use of a larger α_f, the explicit scheme can also adopt a relatively larger time step size. Herein, $\Delta t = 2.5 \times 10^{-4}$ s is adopted for both schemes. Fig. 12 presents the contours of pore pressure. The explicit dynamic FEM results are also presented for comparison. Comparing the pore pressures of 0.05 s and 0.08 s, it is clear that at the initial loading stage, the pressure wave propagates from the loading point to the far end. It then reflects and overlaps after reaching the far-end boundaries (bottom and right). The quantitative comparison shows that even with a larger fluid compressibility, the FSM can also obtain comparable results as the explicit method for 2D problems. Qualitatively, both results are in good agreement with the FEM results. Fig. 13 quantitatively compares the pore pressure and the vertical displacement at point A. Obvious fluctuations are observed from both pressure and displacement evolution curves. Compared to the 1D case, the 2D wave propagation patterns are more complex due to the overlapping of waves from two directions. Notably, the pore pressure magnitude is much smaller than that of the low compressibility case. Although some minor discrepancies between the FSM-based MPM results and the FEM results can be observed, their overall trend and magnitude are quite similar. This example shows that in 2D conditions, the FSM can also effectively capture correct fluid compressibility-related dynamic responses. The

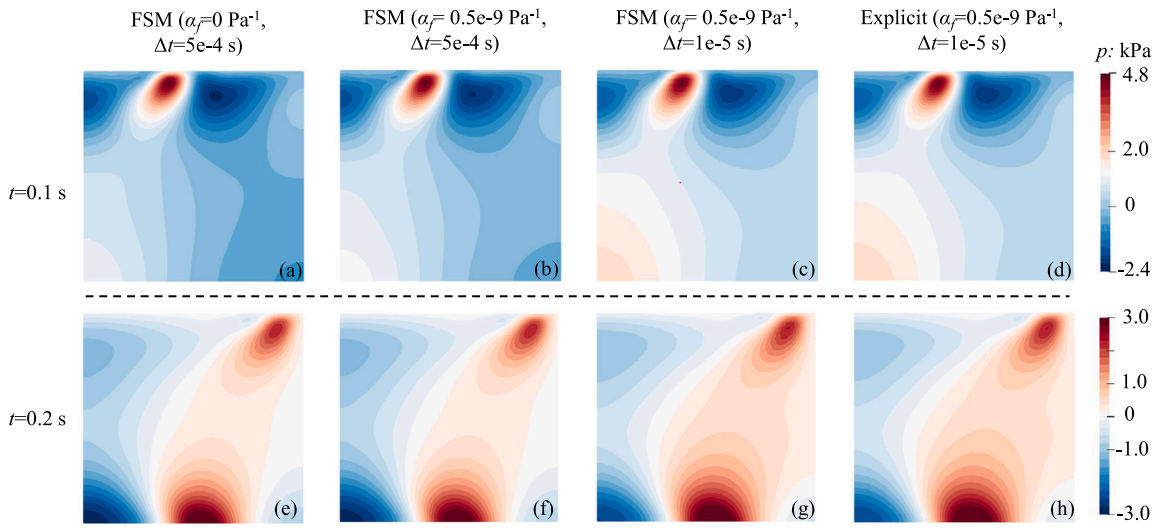

Fig. 11. Pore pressure contours by MPM with FSM and explicit schemes at the time instances of 0.1 s and 0.2 s.

pressure responses in multidimensional conditions are rather complicated, which is dependent on not only the fluid compressibility but also the permeability and the solid stiffness, while a detailed analysis of the wave patterns is out of the scope of this study.

4.2. Thermo-hydro-mechanical coupling problems

The thermal load can also generate pore pressure waves in porous media, though seldom documented in the literature. In this section, 1D and 2D thermo-poroelastic problems are simulated to show how the thermal wave propagates and whether the FSM scheme can capture correct wave features.

4.2.1. 1D thermo-poroelastic response

We first consider a 1D non-isothermal soil column with a height of $H = 1$ m and an initial temperature $T_0 = 0$ °C subjected to a surface temperature increment $T_s = 50$ °C, as illustrated in Fig. 14. The example is modified from the classical non-isothermal consolidation problem designed by Aboustit et al. [59]. It has been widely adopted as a benchmark to validate the THM formulations [23,60–62]. However, the dynamic effect induced by the instantaneously applied thermal load was not investigated in previous works. The model geometry and boundary conditions are basically the same as those of the 1D consolidation case, except that the surface is subject to temperature load. The material properties are given as follows: $\rho_s = 2{,}650$ kg/m^3, $\rho_f = 1{,}000$ kg/m^3, $\phi = 0.4$, $E = 10$ MPa, $\nu = 0.0$, $\mu_f = 1\times10^{-3}$ Pa s, and $k_f = 1\times10^{-10}$ m^2, $c_s = 920$ J/(kg °C), $c_f = 4{,}186$ J/(kg °C), $\lambda_s = 2.4$ MW/(m °C), $\lambda_f = 0.6$ MW/(m °C), $\beta_s = 3\times10^{-5}$ /°C, and $\beta_f = 2.1\times10^{-4}$ /°C. Similarly, the time step size for the explicit scheme is set as $\Delta t = 1\times10^{-5}$ s, whereas for FSM, $\Delta t = 1\times10^{-5}$ and 2.5×10^{-4} s are tested. $\alpha_f = 0.5\times10^{-9}$ Pa^{-1} is first considered, followed by three larger ones, *i.e.*, $\alpha_f = 1\times10^{-8}$, 1×10^{-7}, 1×10^{-6} Pa^{-1}.

Wu [63] gave the analytical solution for this problem under the assumption of incompressible fluid. The temperature T and pore pressure p at time t and depth x and the surface displacement u_s are given as follows,

$$T(x,t) = T_s\left[1 - \sum_{n=0}^{\infty}\frac{2}{\xi H}\sin(\xi x)\cdot e^{-\xi^2\kappa t}\right], \tag{72a}$$

$$p(x,t) = \sum_{n=0}^{\infty}\frac{2}{\xi H}\sin(\xi x)\left[\frac{a-\beta_m M}{1-c/\kappa}T_s(e^{-\xi^2\kappa t} - e^{-\xi^2 c t})\right], \tag{72b}$$

$$u_s(t) = \frac{H}{M}\left[aT_s + \sum_{n=0}^{\infty}\frac{2}{\xi^2 H^2}\left[\frac{a-\beta_m M}{1-c/\kappa}T_s(e^{-\xi^2\kappa t} - e^{-\xi^2 c t}) - aT_s e^{-\xi^2\kappa t}\right]\right], \tag{72c}$$

where $\xi = (2n+1)\pi/(2H)$, $c = k_f M/\rho_l g$ is the consolidation coefficient, $\kappa = \lambda_m/C_m$ is the thermal diffusion coefficient, $b = a - \beta_m M$, $a = \beta_s(3\lambda + 2G)$, $M = \lambda + 2G$, and λ and G are the Lamé constants. For the cases with compressible fluid, the explicit FEM results are also presented for comparison.

Fig. 15(a) shows the evolution of pore pressure at the bottom of the soil column. Similar to the isothermal 1D consolidation example, pressure oscillations are observed at the beginning of the simulation for cases considering fluid compressibility ($\alpha_f = 0.5\times10^{-9}$ Pa^{-1}). Notably, explicit MPM and FEM exhibit stronger temporal oscillations, with the initial pressure peak exceeding 100 kPa and decaying sharply after 0.1 s. In contrast, the FSM-based MPM resolves comparable pressure waves but with significantly

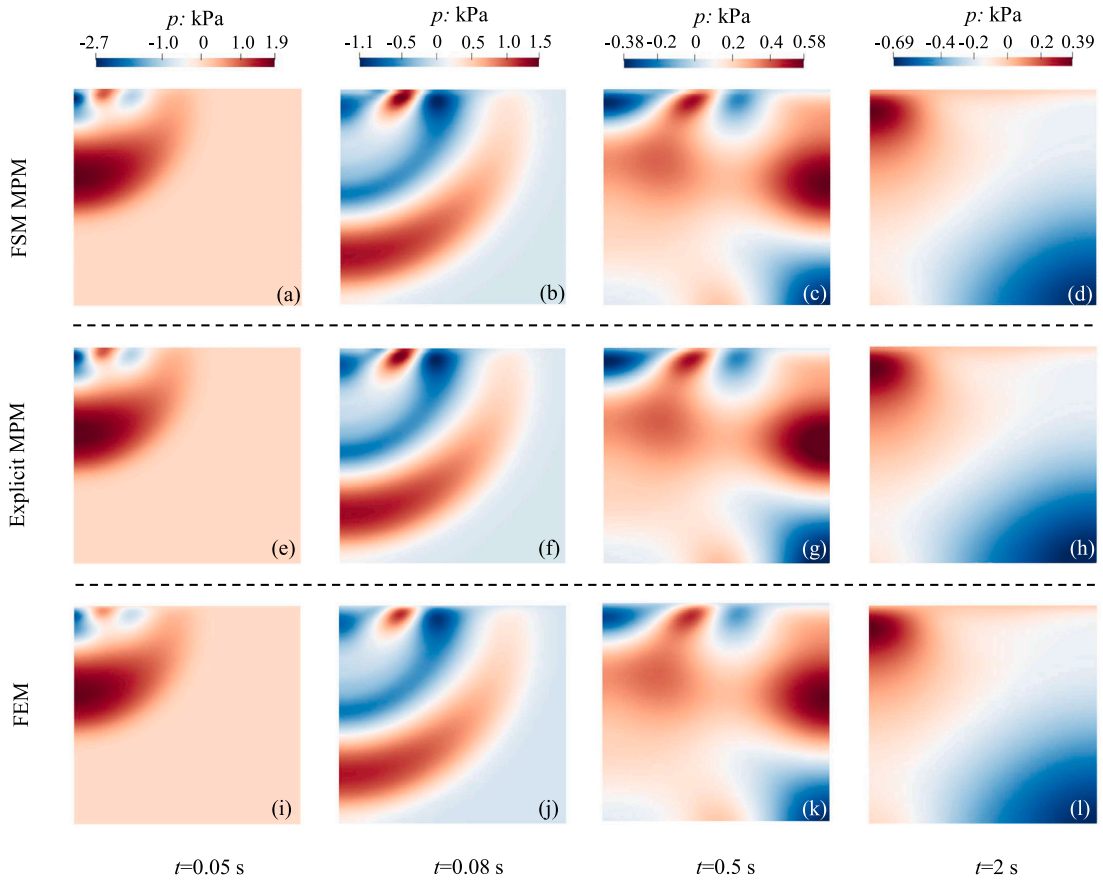

Fig. 12. Comparison of pore pressure solved by (a–d) FSM-based MPM, (e–h) explicit MPM, and (i–l) FEM with fluid compressibility $\alpha_f = 1 \times 10^{-6}$ Pa^{-1} at the time instances of 0.05, 0.08, 0.5, and 2 s.

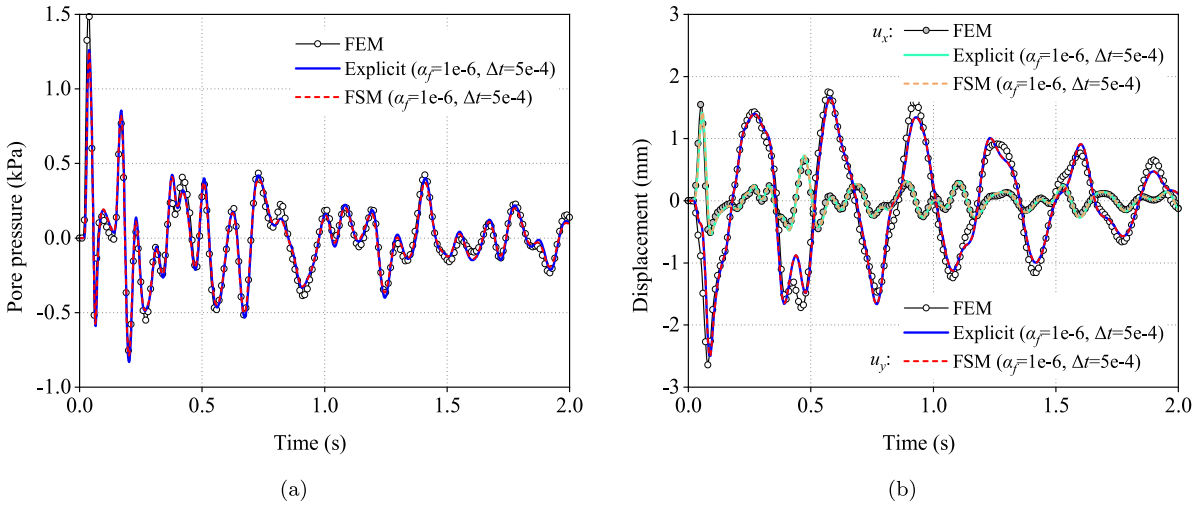

Fig. 13. Evolution of (a) pore pressure and (b) vertical displacement at point A.

stabilized profiles, demonstrating reduced numerical noise and smoother pressure evolution. This suggests the semi-implicit FSM inherently acts as a numerical filter for effective mitigation of high-frequency oscillations through controlled dissipation. However, as the time step Δt increases, the wave peak diminishes, and wave attenuation intensifies, again suggesting that the FSM may fail to

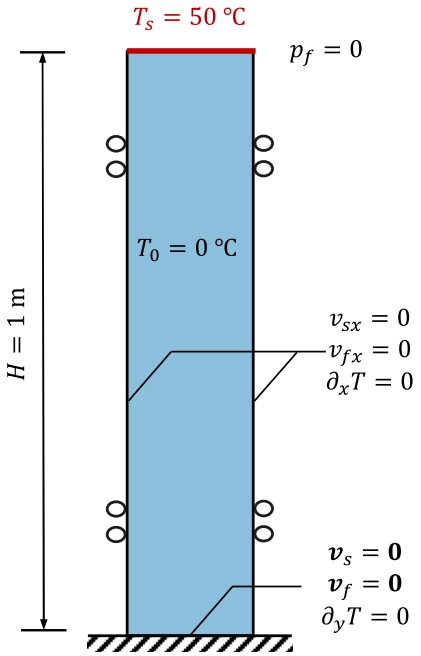

Fig. 14. Geometry and boundary conditions for the 1D thermo-poroelastic problem.

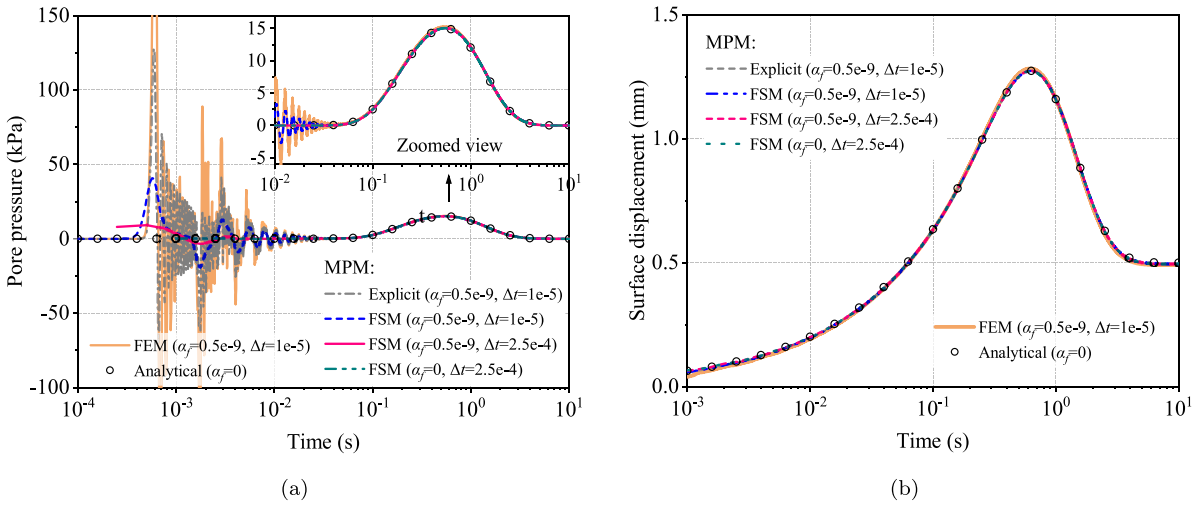

Fig. 15. Evolution of (a) pore pressure at the bottom of the soil column and (b) the surface displacement.

capture the correct wave if the temporal resolution is not fine enough. As pressure waves dampen, a positive pore pressure follows and gradually rises to a peak before dissipating to zero due to fluid drainage from the surface. This behavior arises from solid skeleton expansion due to heating. Throughout this stage, simulated results across all tests closely align with the analytical solution, regardless of the time step size. Furthermore, displacement remains minimally affected by these waves, as evidenced in Fig. 15(b), where simulation curves closely mirror the analytical solution.

Fig. 16 further compares the cases with higher fluid compressibility. For the case with $\alpha_f = 1\times10^{-8}$ Pa^{-1} and $\alpha_f = 1\times10^{-7}$ Pa^{-1}, similar pressure oscillations are observed as the case with $\alpha_f = 0.5\times10^{-9}$ Pa^{-1}. However, as the fluid compressibility increases, the wavelength increases, the amplitude decreases, and the wave attenuation speed decreases as well. Again, employing a large time step for the simulation can accelerate the wave damping. In addition, it is found that for smaller α_f cases, the pressure wave becomes less dominant, whereas the oscillations in the displacement curves seem more evident. Also, with smaller α_f, the peak of pressure and, accordingly, the displacement become smaller compared to the solution for an incompressible fluid. These findings are consistent with the isothermal consolidation cases. In short, thermal load (expansion or contraction) can generate wave propagation akin to

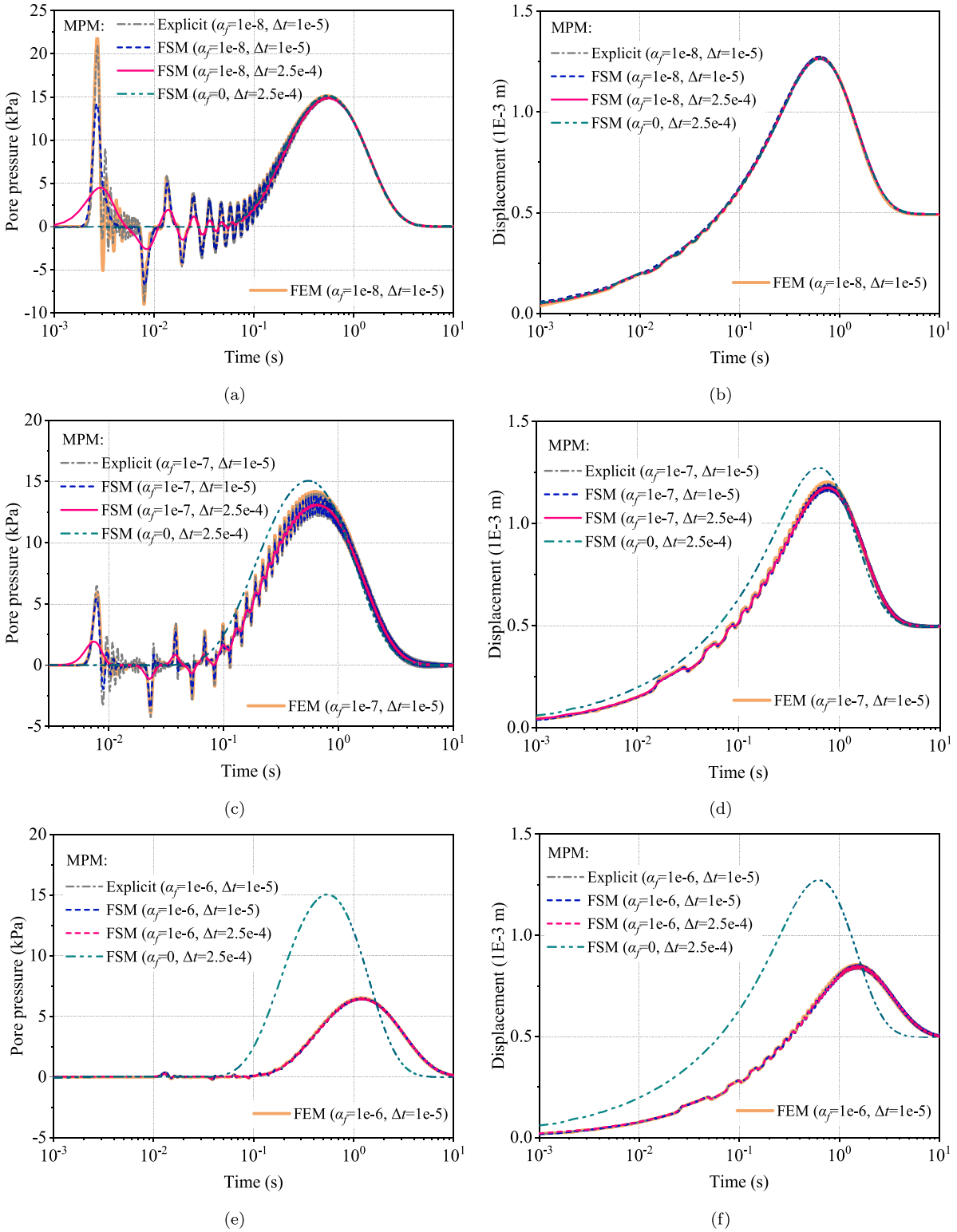

Fig. 16. Evolution of pore pressure at the bottom of the soil column and the surface displacement for (a-b) $\alpha_f = 1 \times 10^{-8}$ Pa^{-1}, (c-d) $\alpha_f = 1 \times 10^{-7}$ Pa^{-1}, and (e-f) $\alpha_f = 1 \times 10^{-6}$ Pa^{-1}.

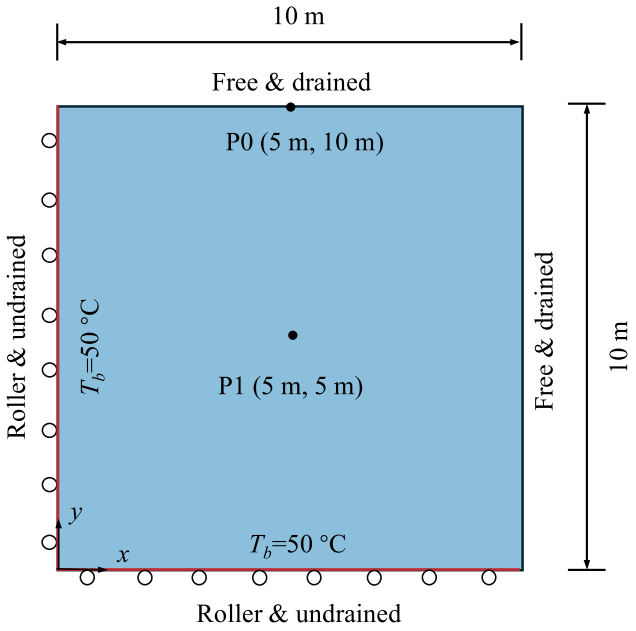

Fig. 17. Geometry and boundary conditions for the 2D thermo-poroelastic problem.

mechanical load, and the wave pattern can be successfully captured if considering the fluid compressibility in FSM when a sufficiently small Δt is used. This indicates that the FSM can be employed for THM modeling of porous media with both incompressible and compressible fluids as explicit dynamics, and the former is even more stable as it can filter some unexpected unphysical oscillations.

4.2.2. 2D thermo-poroelastic wave propagation

The following is a 2D THM example to showcase the dynamic wave propagation in the thermo-poro-elastic condition. Similar cases are presented as benchmarks in literature [64], but no pore fluid is considered. The model geometry and boundary conditions are depicted in Fig. 17. A square domain of 10 m × 10 m with an initial temperature of 0 °C is simulated. The left and bottom sides are fixed in normal directions and are prescribed with a fixed temperature of 50 °C. The two boundaries are impermeable, while the other two are free-drained boundaries. The material domain is discretized into 2,500 quadrilateral cells with a uniform size of 0.2 m, and four particles are initiated in each cell. The material is modeled as perfectly linear elastic and the material parameters are given as follows: ρ_s = 2,650 kg/m^3, ρ_f = 1,000 kg/m^3, ϕ = 0.4, E = 10 MPa, ν = 0.0, $\mu_f = 1\times10^{-3}$ Pa s, and $k_f = 1\times10^{-10}$ m^2, c_s = 4,186 J/(kg °C), c_f = 920 J/(kg °C), λ_s = 2.4 MW/(m °C), λ_f = 0.6 MW/(m °C), $\beta_s = 3\times10^{-5}$ /°C, and $\beta_f = 2.1\times10^{-4}$ /°C. Two fluid compressibilities are considered, *i.e.*, $\alpha_f = 0.5\times10^{-9}$ Pa^{-1} and $\alpha_f = 1\times10^{-7}$ Pa^{-1}.

Fig. 18 compares the spatial distribution of thermal-induced pore pressure. After the application of the thermal load, two orthogonal pressure waves are initiated from the fixed end and propagate to the free end. Overlapping of the two waves yields an evident peak alongside the 45-degree zone, propagating to the free end and then splitting into two again. The quantitative comparison shows that the FSM can capture the same dynamic wave pattern as the explicit scheme. Fig. 19(a) qualitatively shows the evolution of pore pressure at the central point P1 (5 m, 5 m) of the domain, which approximately follows a gradually damped sinusoidal wave. Both schemes give the same simulation results with $\alpha_f = 0.5\times10^{-9}$ Pa^{-1}. Again, if we set $\alpha_f = 0$, the FSM cannot capture such pressure waves. Normally, there are two sources of pressure: one is fluid compressibility-induced pressure, and the other is thermal expansivity-induced pressure. However, for the case with $\alpha_f = 0.5\times10^{-9}$ Pa^{-1}, the latter effect is less significant compared to the former at the initial loading stage, although some indications can still be found at the left-bottom corner at t = 0.0055 s in Fig. 18. Fig. 19(b) plots the vertical displacement at P0 (5 m, 10 m). Again, FSM with $\alpha_f = 0.5\times10^{-9}$ Pa^{-1} captures some wave patterns that FSM with $\alpha_f = 0$ cannot. Except for some local displacement oscillations corresponding to the pressure waves, there are still three obvious waves on a larger time scale induced by the thermal expansion.

Fig. 20 shows the contour results of pore pressure in the case with $\alpha_f = 1\times10^{-7}$ Pa^{-1}. Again, FSM can capture the same pressure pattern as the explicit method. The pressure pattern shown in Fig. 20, especially the two orthogonal waves, is rather similar to that in Fig. 18. However, the magnitude of the pressure wave is much lower than that of the low compressibility case. As a consequence, the pressure increment near the left and bottom boundaries, the thermal expansion-induced pore pressure, becomes more evident. Fig. 21 compares the time evolution of pore pressure at P1 and vertical displacement at P0 solved by explicit and semi-implicit MPM. Both results are nearly identical to each other. Obviously, the 2D thermal wave propagation is more complex than the 1D case. The details of the wave patterns will not be discussed in further detail since it is beyond the scope of this study.

To this stage, we have presented rich examples to demonstrate the efficacy of FSM in capturing the mechanical and thermal-induced pressure wave in porous media with compressible fluid, but all are in the elastic range.

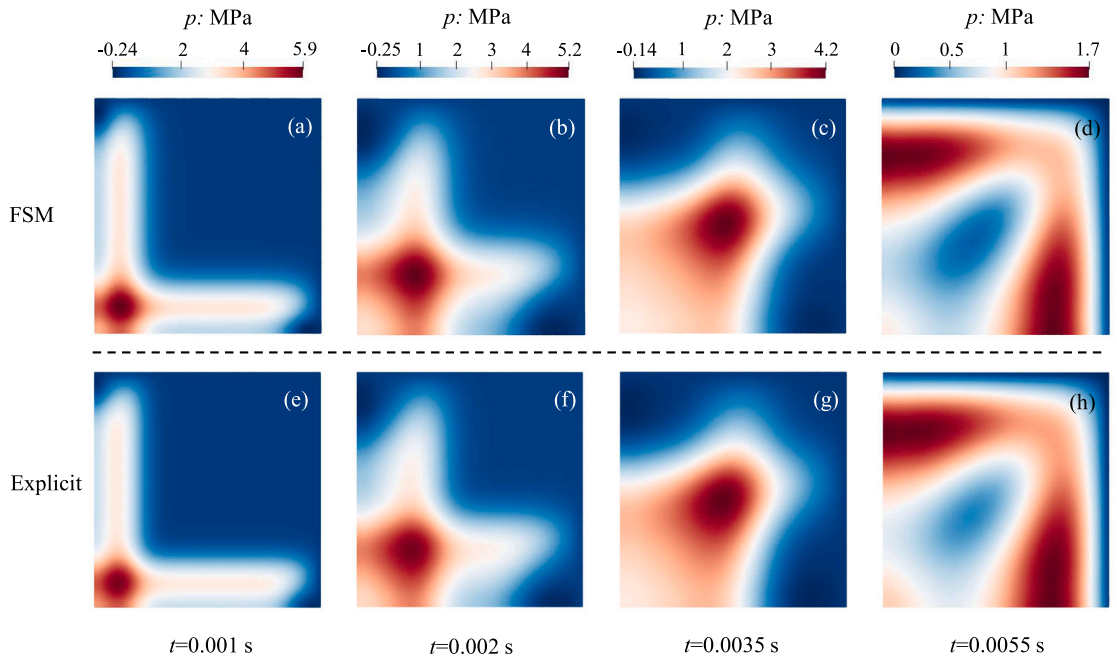

Fig. 18. Comparison of thermal-induced wave propagation in porous media simulated by coupled MPM based on (a–d) FSM and (e–h) exlicit schemes at four representative time instances.

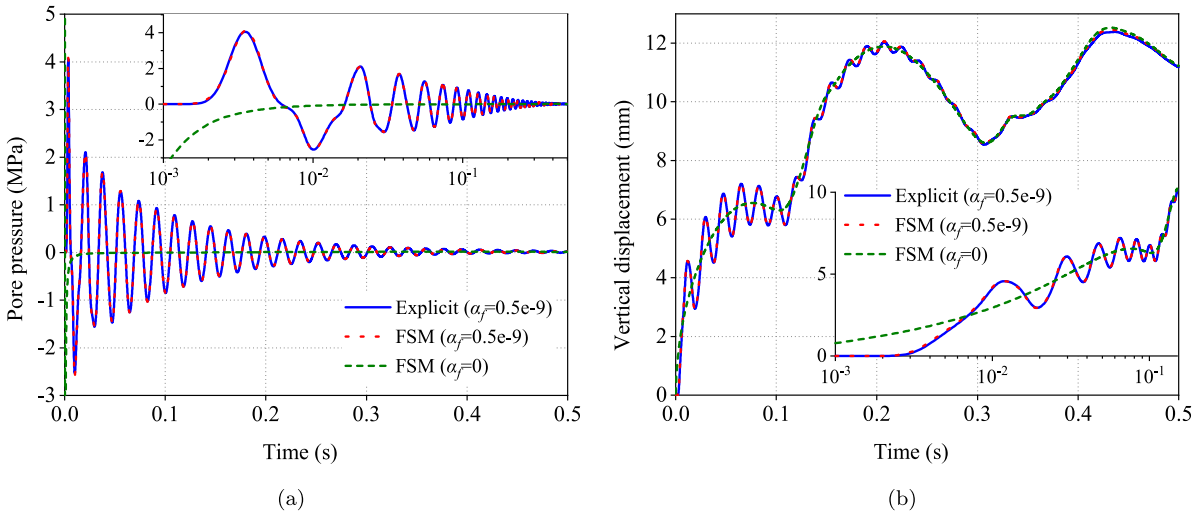

Fig. 19. (a) Thermal-induced pore pressure at the central point P1 (5 m, 5 m) and (b) vertical displacement at point P0 (5 m, 10 m) on the top surface.

4.3. Progressive failure of a slope

The last example simulates the progressive failure of a sensitive slope to show that the compressible FSM can correctly simulate the large deformation and failures in geotechnical problems. The geometry and boundary conditions are depicted in Fig. 22a. The height and bottom length are 5 m and 20 m, respectively, and the slope angle is 45°. The bottom is fixed as a no-slip boundary, and the left is a roller boundary. The soil slope is assumed to be saturated, and no external heat source is applied. Quadrilateral mesh is used with a uniform mesh size of 0.2 m and initially four material points in each grid cell. The slope is consolidated first under gravity. During the consolidation stage, the linear elastic material model is adopted, with the material properties as follows: $\rho_s = 2{,}040\ \mathrm{kg/m^3}$, $\rho_f = 1{,}000\ \mathrm{kg/m^3}$, $\phi = 0.4$, $\alpha_f = 0$, $E = 1$ MPa, and $\nu = 0.33$. To accelerate the consolidation process, a large permeability $k_f = 1\times10^{-6}\ \mathrm{m^2}$ is adopted. The pore pressure after consolidation is presented in Fig. 22b. Then, the pore pressure and the initial stress serve as the initial conditions for the following slope failure simulation. The linear strain-softening Mohr–Coulomb

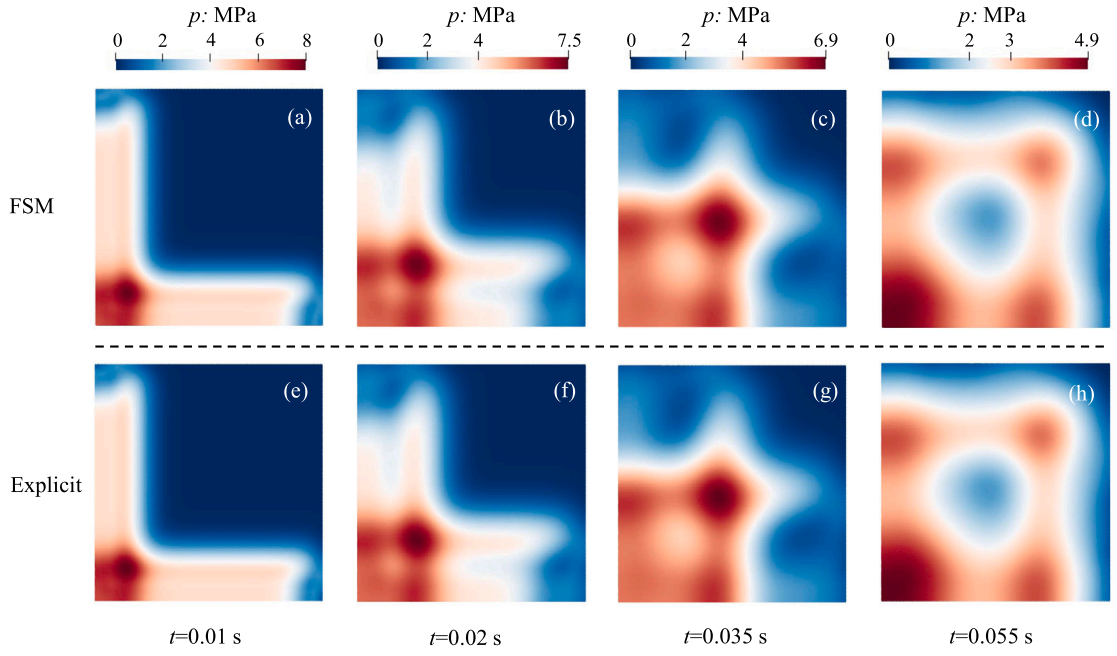

Fig. 20. Comparison of thermal-induced wave propagation in porous media simulated by (a-d) FSM and (e-h) explicit schemes.

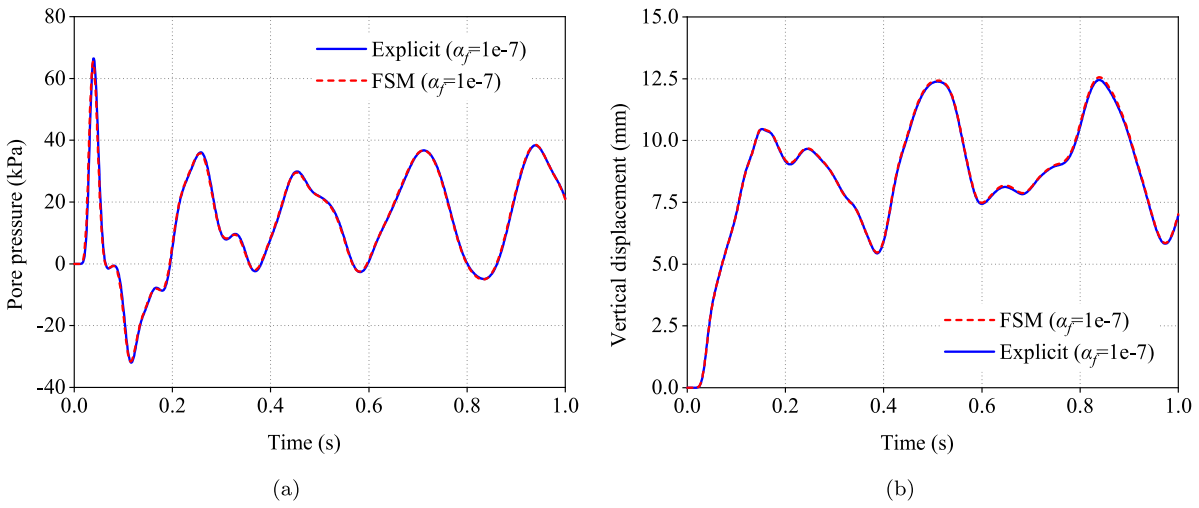

Fig. 21. Comparison of thermal-induced wave propagation in porous media simulated by explicit MPM and FSM-based semi-implicit MPM: (a) pore pressure at P1 and (b) vertical displacement at P0.

model is adopted, with the strength parameter as follows: initial peak shear strength $\varphi_{peak} = 10°$ and $c_{peak} = 15$ kPa, residual shear strength $\varphi_{res} = 0.5°$ and $c_{res} = 2$ kPa, residual plastic deviatoric strains $\epsilon^p_{res} = 0.2$, and the peak plastic deviatoric strain $\epsilon^p_{peak} = 0$. The permeability is set as $k_f = 1 \times 10^{-15}$ m^2, and the fluid compressibility is set as $\alpha_f = 1 \times 10^{-8}$ Pa^{-1}. Both the explicit scheme and the FSM are tested for comparison purposes. It is worth mentioning that the PIC damping will cause extra energy dissipation, and the total amount of energy loss in a simulation round is dependent on the magnitude of the PIC damping coefficient α_{PIC} and the time step. Therefore, for a fair comparison, both schemes adopt the same time step size of 5×10^{-4} s and the same $\alpha_{PIC} = 0.001$.

Fig. 23 shows the progressive failure process. There are three major slope slide events occurring at about 0.75. 3.25, and 6.5 s. For each slide, there is a major shear band accompanied by one or several minor shear bands. The explicit MPM is also employed to simulate the same problem, as shown in Fig. 24. Also, there are three slope slide events with the occurring times and locations and failure patterns nearly the same as those of the FSM results, except that the shear bands in the second slide show minor differences. For both simulations, the slope slides finally stopped with a runout of 27.5 m and a retrogressive distance of about 20 m. Fig. 25 and Fig. 26 further show the contours of pore pressure at the time of each slide initiation solved based on the FSM and explicit

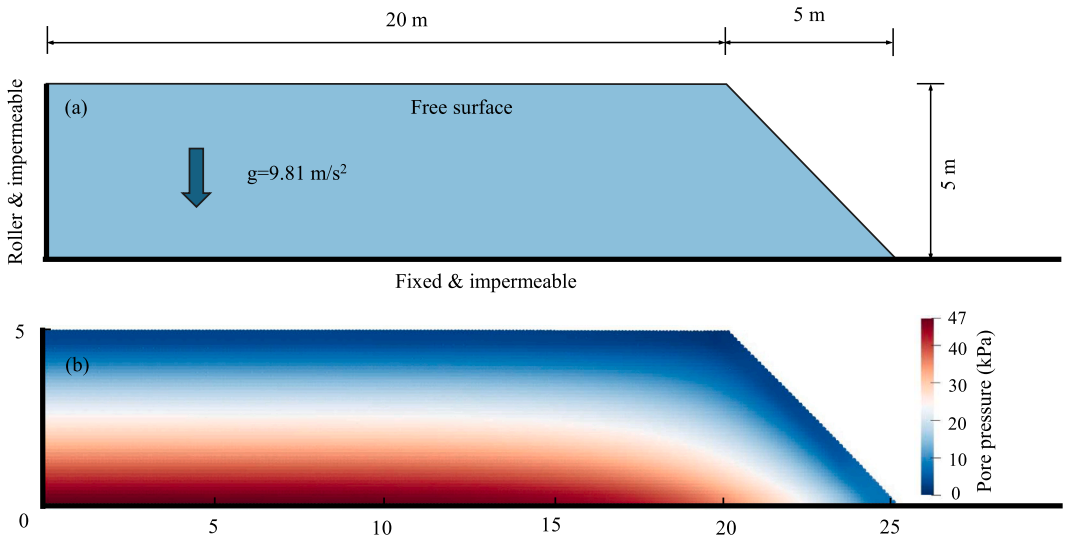

Fig. 22. (a) Geometry and boundary condition of a saturated slope, and (b) pore pressure after self-weight consolidation.

schemes. It is found that the pore pressure below the arc-shaped shear band in the slide event will increase suddenly, while above the shear band, the pore pressure decreases. Apparently, the pore pressures solved by both schemes are almost identical. Fig. 27 compares the kinetic energy of the soil slope during the progressive failure process. Three peaks can be observed, corresponding to the three slides. The evolution curves for FSM and explicit MPM demonstrate close agreement. However, explicit MPM exhibits slower energy damping compared to FSM. This discrepancy likely stems from differences in shear band formation during the second sliding event, where distinct pressure field solution schemes (semi-implicit FSM vs. explicit) may drive divergence in shear band bifurcation. Additionally, numerical instability (*e.g.*, mesh distortion, hourglassing) may accumulate errors over time, leading to divergent kinetic energy evolution paths. For small-deformation problems (discussed in prior sections), these factors have a negligible impact, resulting in nearly identical FSM and explicit MPM results. However, in large deformation regimes, perturbations from pressure field approximations and instability mechanisms are amplified temporally and spatially, culminating in a bifurcation point at a critical time frame. Overall, the FSM-based MPM can capture similar results as the explicit dynamics for a large deformation slope failure case if the fluid compressibility is set. Therefore, the FSM can be extended to simulate large deformations in porous media with compressible fluid.

To demonstrate the influence of fluid compressibility on the slope failure patterns, we compared the post-failure patterns of four cases with $\alpha_f = 1\times10^{-9}$, 1×10^{-8}, 1×10^{-7}, and 1×10^{-6} Pa^{-1}, labeled as Case 1, Case 2, Case 3, and Case 4, respectively. Fig. 28 depicts the deviatoric strains, which also shows the final slope geometry after the progressive failure. Similar to Case 2, Case 1 also experiences three major retrogressive slides. However, the runout distance and the retrogressive distance in Case 1 are a bit longer than in Case 2. By contrast, Case 3 experiences only two major retrogressive slides, and Case 4 only one major slide with a minor slide. Consequently, the retrogressive distances in Case 3 and Case 4, which are about 13.5 and 11.5 m, respectively, are much less than those in Case 1 and Case 2. The distinct responses result from the pore pressure, which is normally larger in the low α_f porous media than in the high α_f media. Inversely, the effective stress in the former case is lower than in the latter case. Therefore, the low α_f case is more prone to retrogressive failures. This example demonstrates the significance of considering pore fluid compressibility in accurately simulating the slope instability response.

5. Discussion on extension of three-phase fractional step formulation

While the FSM has proven effective for dynamic analysis of porous media with compressible fluids under the simplification of homogenized fluid–solid mixtures, it does not inherently resolve liquid/gas saturation evolutions or capillary suction in triphasic systems. These effects are critical for modeling unsaturated soils. To bridge the gap, we extend the two-phase FSM to a three-phase framework, a novel advancement not yet reported in literature due to challenges in operator-splitting of three velocities variables ($\boldsymbol{v}_s$, $\boldsymbol{v}_l$, $\boldsymbol{v}_g$) and two pressure variables (p_l, p_g). To tackle this challenge, we herein introduce three intermediate velocities ($\boldsymbol{v}_s^*$, $\boldsymbol{v}_l^*$, $\boldsymbol{v}_g^*$) and solve two incremental pressures (Δp_l^{k+1} and Δp_g^{k+1}). Although this treatment will inevitably increase the degree of freedom of the linear system, the computational cost remains manageable due to the node-based implicit scheme for intermediate velocities. This section outlines the three-phase fractional step formulation under isothermal conditions (non-isothermal extensions follow analogously) and validates its efficacy through simplified benchmarks.

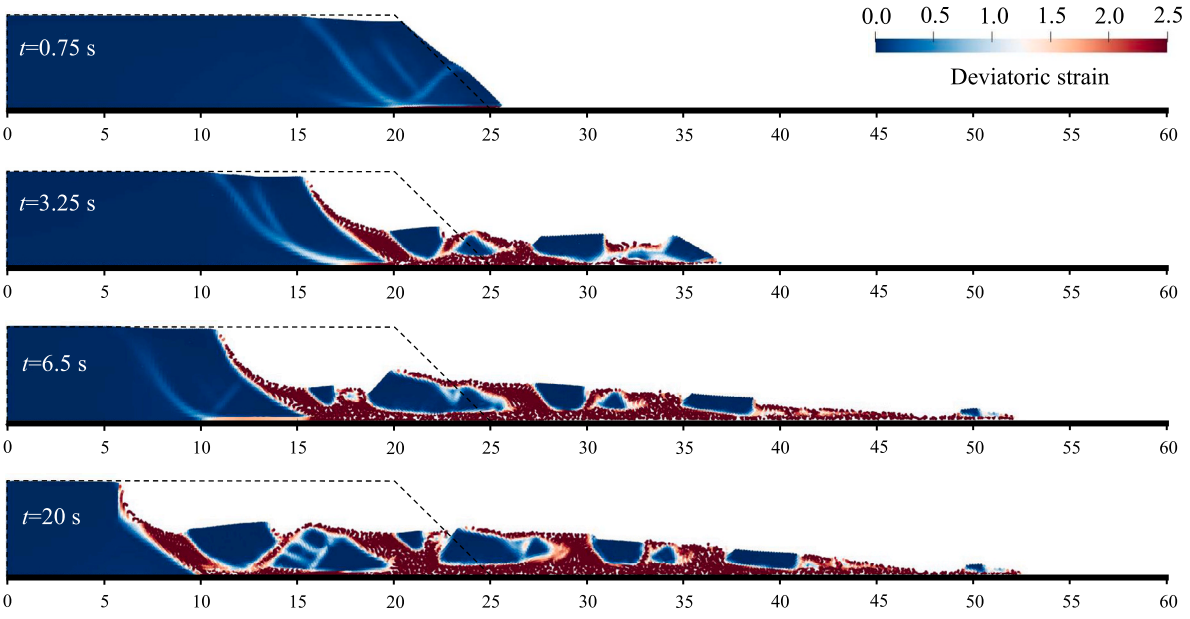

Fig. 23. Contours of deviatoric strain simulated by coupled MPM based on FSM with $\alpha_f = 1 \times 10^{-8}$ Pa^{-1} at the time instances of 0.75, 3.25, 6.5, and 20 s.

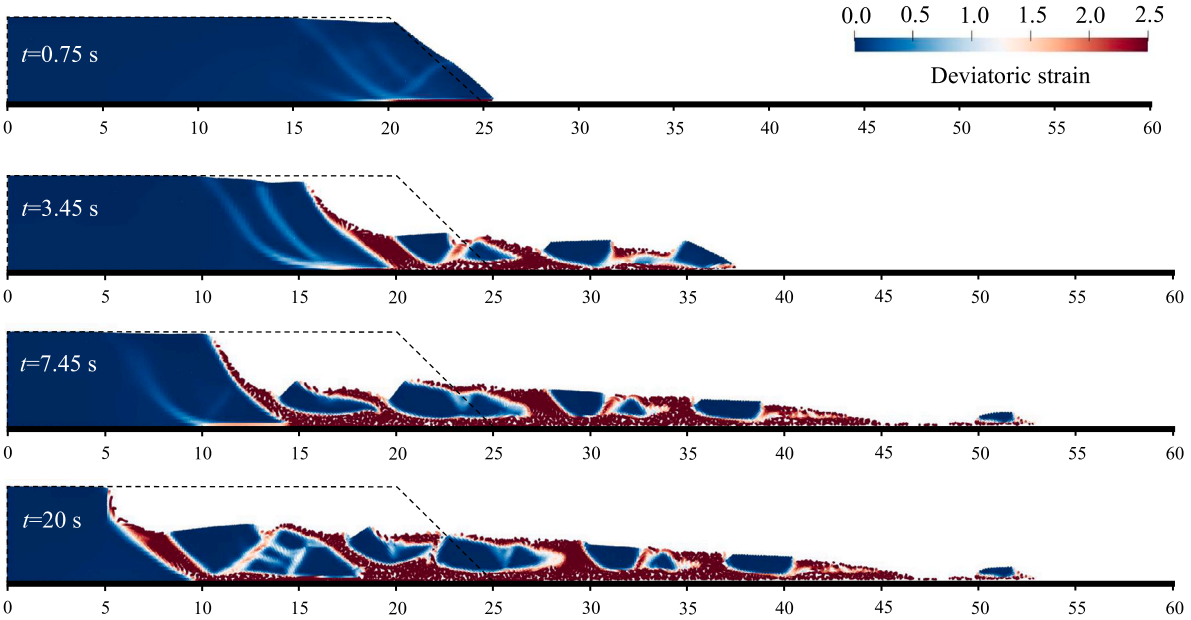

Fig. 24. Contours of deviatoric strain simulated by coupled MPM based on explicit scheme with $\alpha_f = 1 \times 10^{-8}$ Pa^{-1} at the time instances of 0.75, 3.45, 7.45, and 20 s.

5.1. Three-phase material point method based on fractional step method

First, we split the momentum balance equations of the mixture, liquid, and gas phases, by introducing three intermediate velocities, $\boldsymbol{v}_s^*$, $\boldsymbol{v}_l^*$, and $\boldsymbol{v}_g^*$, into the predictors:

$$(1-\phi)\rho_s \dot{\boldsymbol{v}}_s^* + \phi S_l \rho_l \dot{\boldsymbol{v}}_l^* + \phi S_g \rho_g \dot{\boldsymbol{v}}_g^* = \nabla \cdot \boldsymbol{\sigma}'^k - \nabla \left(S_l p_l^k + S_g p_g^k \right) + \rho_m \boldsymbol{b}, \tag{73a}$$

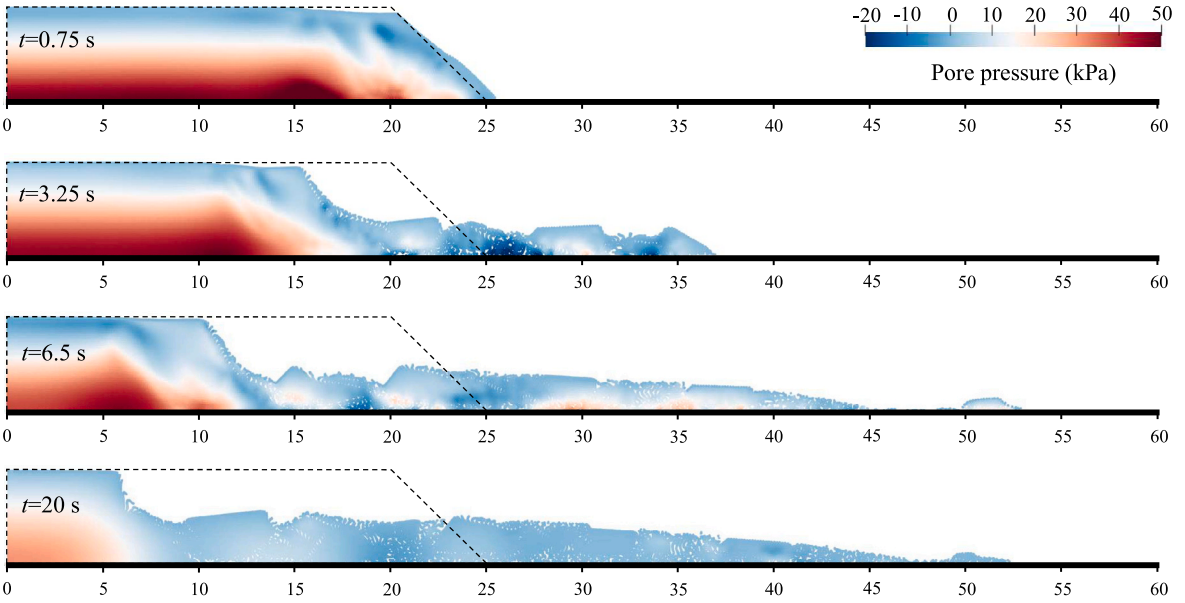

Fig. 25. Contours of pore pressure simulated by coupled MPM based on FSM with $\alpha_f = 1 \times 10^{-8}$ Pa^{-1} at the time instances of 0.75, 3.25, 6.5, and 20 s.

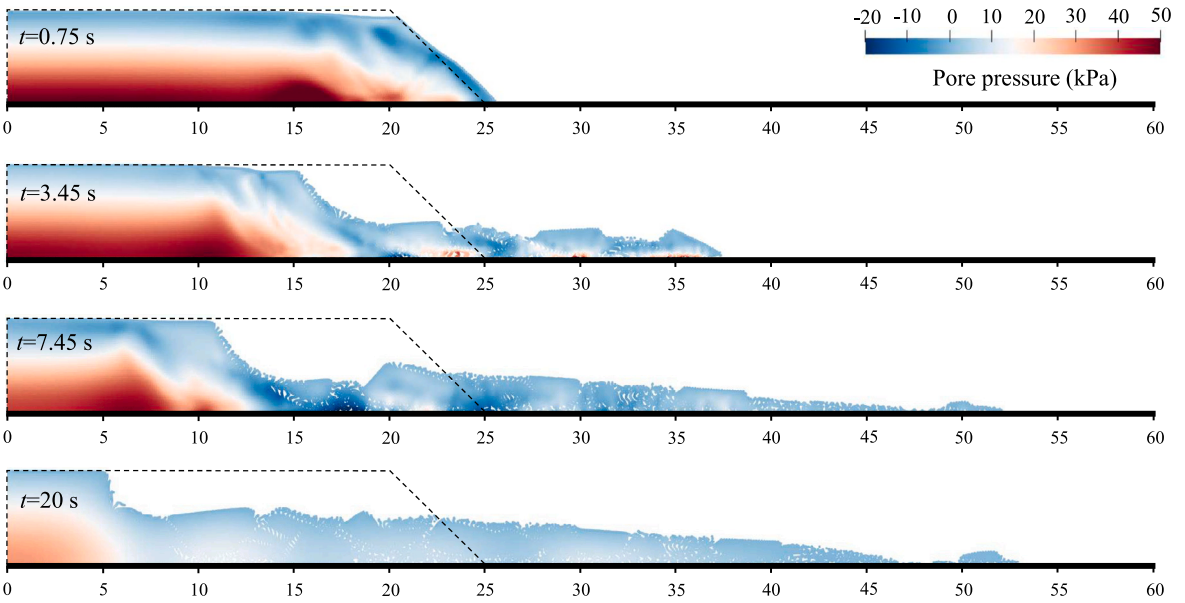

Fig. 26. Contours of pore pressure simulated by coupled MPM based on explicit scheme with $\alpha_f = 1 \times 10^{-8}$ Pa^{-1} at the time instances of 0.75, 3.45, 7.45, and 20 s.

$$\phi S_l \rho_l \dot{\boldsymbol{v}}_l^* = -\phi S_l \nabla p_l^k + \phi S_l \rho_l \boldsymbol{b} - (\phi S_l)^2 \frac{\mu_l}{k_a k_{rl}} (\boldsymbol{v}_l^* - \boldsymbol{v}_s^*), \tag{73b}$$

$$\phi S_g \rho_g \dot{\boldsymbol{v}}_g^* = -\phi S_g \nabla p_g^k + \phi S_g \rho_g \boldsymbol{b} - (\phi S_g)^2 \frac{\mu_g}{k_a k_{rg}} (\boldsymbol{v}_g^* - \boldsymbol{v}_s^*), \tag{73c}$$

and the correctors:

$$(1-\phi)\rho_s \dot{\boldsymbol{v}}_s^{**} = -(1-\phi) S_l \nabla(\Delta p_l^{k+1}) - (1-\phi) S_g \nabla(\Delta p_g^{k+1}), \tag{74a}$$

$$\phi S_l \rho_l \dot{\boldsymbol{v}}_l^{**} = -\phi S_l \nabla(\Delta p_l^{k+1}), \tag{74b}$$

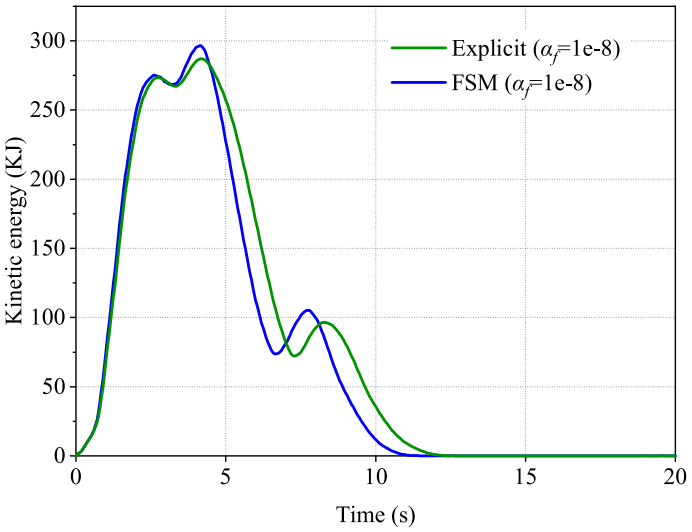

Fig. 27. Evolution of kinematic energy during the progressive slope failure.

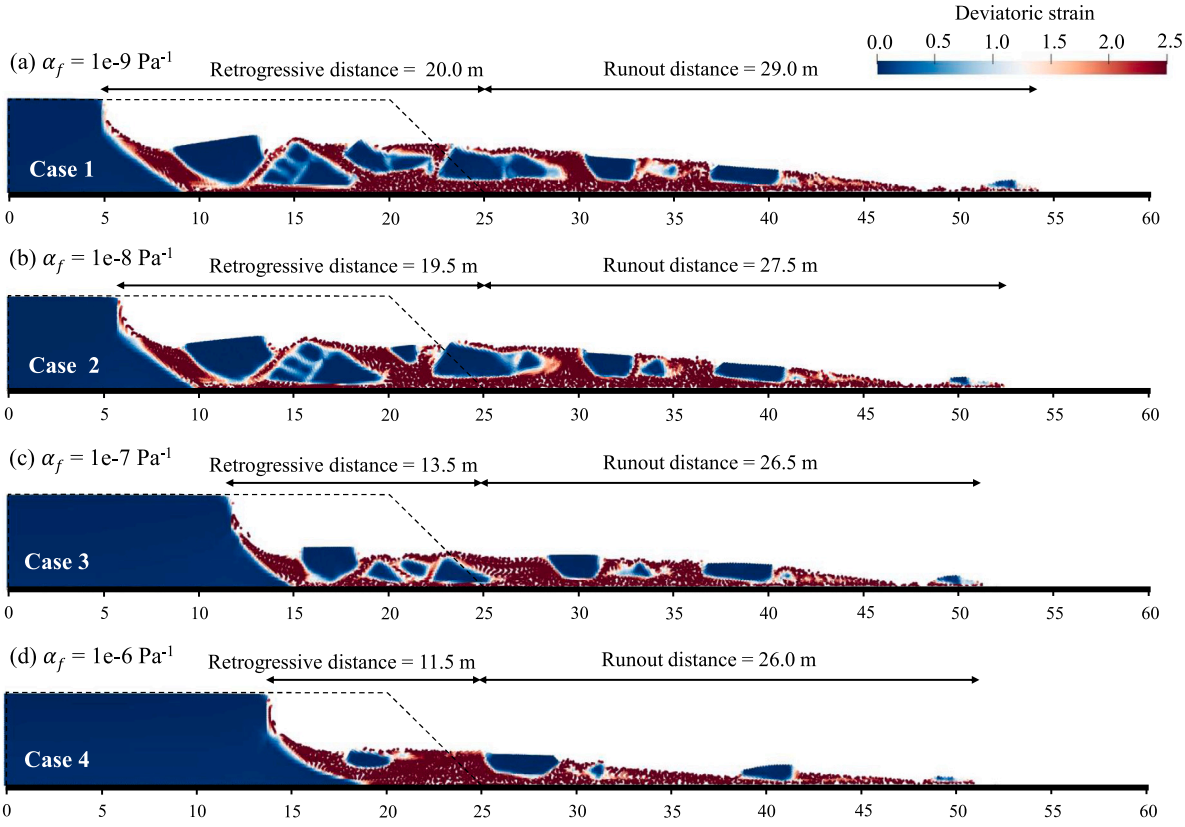

Fig. 28. Comparison of progressive slope failures with (a) $\alpha_f = 1 \times 10^{-9}$ Pa^{-1}, (b) $\alpha_f = 1 \times 10^{-8}$ Pa^{-1}, (c) $\alpha_f = 1 \times 10^{-7}$ Pa^{-1}, and (d) $\alpha_f = 1 \times 10^{-6}$ Pa^{-1}.

$$\phi S_g \rho_g \dot{\boldsymbol{v}}_g^{**} = -\phi S_g \nabla(\Delta p_g^{k+1}). \tag{74c}$$

where $\Delta p_l^{k+1} = p_l^{k+1} - p_l^k$ and $\Delta p_g^{k+1} = p_g^{k+1} - p_g^k$. Note that the drag force correction terms are ignored here for simplicity.

Building on the two-phase FSM derivation framework, we substitute the three-phase correctors (Eq. (74)) into the mass conservation equation (Eq. (13)) to derive the pressure Poisson equations for the liquid and gas phases:

$$S_l\Delta t\left(\frac{1-\phi}{\rho_s}S_l+\frac{\phi}{\rho_l}\right)\nabla^2(\Delta p_l^{k+1})+S_l\Delta t\frac{1-\phi}{\rho_s}S_g\nabla^2(\Delta p_g^{k+1})-\phi\frac{\partial S_l}{\partial p_c}\dot{p}_g^{k+1}-\left(\phi S_l\alpha_l-\phi\frac{\partial S_l}{\partial p_c}\right)\dot{p}_l^{k+1}= S_l\nabla\cdot\boldsymbol{v}_s^*+\phi S_l\nabla\cdot(\boldsymbol{v}_l^*-\boldsymbol{v}_s^*), \tag{75a}$$

$$S_g\Delta t\left(\frac{1-\phi}{\rho_s}S_g+\frac{\phi}{\rho_g}\right)\nabla^2(\Delta p_g^{k+1})+S_g\Delta t\frac{1-\phi}{\rho_s}S_l\nabla^2(\Delta p_l^{k+1})+\phi\frac{\partial S_g}{\partial p_c}\dot{p}_l^{k+1}-\left(\phi S_g\alpha_g+\phi\frac{\partial S_g}{\partial p_c}\right)\dot{p}_g^{k+1}= S_g\nabla\cdot\boldsymbol{v}_s^*+\phi S_g\nabla\cdot(\boldsymbol{v}_g^*-\boldsymbol{v}_s^*). \tag{75b}$$

The weak form is derived using the standard Galerkin method; its detailed formulation is omitted here for brevity. The node-based implicit scheme is retained to solve the momentum balance equations to ensure computational efficiency. Following the temporal solution sequence, the final discretized form for each time step is outlined below:

(1) Predictor of momentum equations to solve $\dot{\boldsymbol{v}}_s^*$, $\dot{\boldsymbol{v}}_l^*$, and $\dot{\boldsymbol{v}}_g^*$:

$$\begin{bmatrix}\mathcal{M}_s & \mathcal{M}_l & \mathcal{M}_g\\ -\Delta t\mathcal{Q}_l^d & \mathcal{M}_l+\Delta t\mathcal{Q}_l^d & 0\\ -\Delta t\mathcal{Q}_g^d & 0 & \mathcal{M}_g+\Delta t\mathcal{Q}_g^d\end{bmatrix}_I\begin{Bmatrix}\dot{\boldsymbol{v}}_s^*\\ \dot{\boldsymbol{v}}_l^*\\ \dot{\boldsymbol{v}}_g^*\end{Bmatrix}_I=\begin{Bmatrix}\boldsymbol{f}^{ext}+\boldsymbol{f}^{int}\\ \boldsymbol{f}_l^{ext}+\boldsymbol{f}_l^{int}-\mathcal{Q}_l^d(\boldsymbol{v}_l^k-\boldsymbol{v}_s^k)\\ \boldsymbol{f}_g^{ext}+\boldsymbol{f}_g^{int}-\mathcal{Q}_g^d(\boldsymbol{v}_g^k-\boldsymbol{v}_s^k)\end{Bmatrix}_I. \tag{76}$$

(2) Pressure Poisson equation to solve Δp_l^{k+1} and Δp_g^{k+1}

$$\begin{bmatrix}\mathcal{L}_{ll}+\mathcal{K}_{ll} & \mathcal{L}_{lg}+\mathcal{K}_{lg}\\ \mathcal{L}_{gl}+\mathcal{K}_{gl} & \mathcal{L}_{gg}+\mathcal{K}_{gg}\end{bmatrix}\begin{Bmatrix}\Delta p_l^{k+1}\\ \Delta p_g^{k+1}\end{Bmatrix}=\begin{Bmatrix}\boldsymbol{\mathcal{F}}_{ls}\cdot\boldsymbol{v}_s^*+\boldsymbol{\mathcal{F}}_{ll}\cdot(\boldsymbol{v}_l^*-\boldsymbol{v}_s^*)\\ \boldsymbol{\mathcal{F}}_{gs}\cdot\boldsymbol{v}_s^*+\boldsymbol{\mathcal{F}}_{gg}\cdot(\boldsymbol{v}_g^*-\boldsymbol{v}_s^*)\end{Bmatrix}. \tag{77}$$

(3) Corrector of momentum equations to solve $\dot{\boldsymbol{v}}_s^{k+1}$, $\dot{\boldsymbol{v}}_l^{k+1}$, and $\dot{\boldsymbol{v}}_g^{k+1}$:

$$\begin{bmatrix}\mathcal{M}_s & 0 & 0\\ 0 & \mathcal{M}_l & 0\\ 0 & 0 & \mathcal{M}_g\end{bmatrix}\begin{Bmatrix}\dot{\boldsymbol{v}}_s^{k+1}\\ \dot{\boldsymbol{v}}_l^{k+1}\\ \dot{\boldsymbol{v}}_g^{k+1}\end{Bmatrix}=\begin{Bmatrix}\boldsymbol{\mathcal{N}}_{sl}(\Delta p_l^{k+1})+\boldsymbol{\mathcal{N}}_{sg}(\Delta p_g^{k+1})+\mathcal{M}_s\dot{\boldsymbol{v}}_s^*\\ \boldsymbol{\mathcal{N}}_{ll}(\Delta p_l^{k+1})+\mathcal{M}_l\dot{\boldsymbol{v}}_l^*\\ \boldsymbol{\mathcal{N}}_{gg}(\Delta p_g^{k+1})+\mathcal{M}_g\dot{\boldsymbol{v}}_g^*\end{Bmatrix}. \tag{78}$$

The expressions of the matrices in the above linear equation sets are presented in Appendix.

5.2. Numerical example: 1D consolidation of unsaturated porous media

We first validate the model by simulating suction-induced consolidation of an unsaturated porous medium within the elastic regime. The benchmark replicates with work of Lei et al. [23], who employed an explicit two-phase MPM with a simplified $\boldsymbol{v}_s-\boldsymbol{v}_l-p_l$ formulation assuming zero gas pressure ($p_g=0$). Here is the model setup: A 1 m tall soil column (Fig. 2) is initialized with homogeneous matric suction $p_c=300$ kPa and liquid saturation $S_l=0.7$, governed by a linear soil–water retention curve (SWRC): $p_c=10^6(1-S_l)$ Pa. A suction increase to 500 kPa is applied instantaneously at the top boundary at the beginning of the simulation. The material properties are give as follows: solid density $\rho_s=2{,}500$ kg/m^3, liquid density $\rho_l=1{,}000$ kg/m^3, gas molar mass $M_g=0.029$ kg/mol, porosity $\phi=0.3$, liquid compressibility $\alpha_l=0.5\times10^{-9}$ Pa^{-1}, Young's modulus $E=10$ MPa, Poisson's ratio $\nu=0.4$, liquid viscosity $\mu_l=1\times10^{-3}$ Pa s, gas viscosity $\mu_g=1\times10^{-5}$ Pa s, and absolute permeability $k_a=5\times10^{-11}$ m^2. The simulation uses a time step size of 1×10^{-4} s under isothermal conditions.

For direct comparison with Lei et al. [23], we first enforce a constant pore gas pressure ($p_g=100$ kPa) for a reduced $\boldsymbol{v}_s-\boldsymbol{v}_l-p_l$ formulation. Fig. 29 compares spatial distributions of suction (p_c), liquid saturation (S_l), porosity (ϕ), and vertical displacement at four time instances. The results show that saturation undergoes a gradual reduction from 0.7 to 0.5 due to the suction effect, and porosity drops slightly due to consolidation. The spatial distributions of the four variables exhibit strong agreement with Lei et al. [23]'s results, validating our model's accuracy. Note: Porosity in Lei et al. [23] is extrapolated from volumetric strain (ε_v) by $\phi=(\phi_0+\varepsilon_v)/(1+\varepsilon_v)$, where ϕ_0 is initial porosity.

To advance the analysis, we further simulate the same problem using the three-phase FSM based on $\boldsymbol{v}_s-\boldsymbol{v}_l-\boldsymbol{v}_g-p_l-p_g$ formulation. Pore gas pressure in the soil column is allowed to dynamically evolve during consolidation while maintaining a fixed surface gas pressure at 100 kPa due to drainage. This framework incorporates saturation-dependent permeability, which is absent in Lei et al. [23]'s work, using the following Brooks–Corey model, [49,65]:

$$k_{rl}=S_e^{3+2m},\quad k_{rg}=(1-S_e)^2\left(1-S_e^{1+2m}\right), \tag{79}$$

where $S_e=(S_l-S_{lc})/(1-S_{lc})$ is the effective saturation, S_{lc} is the irreducible water saturation, and m is the pore size distribution index. S_{lc} and m are taken as 0 and 0.3, respectively, in this example. Fig. 30 shows the temporal evolution of suction (p_c), pore gas pressure (p_g), and pore liquid pressure (p_l) at the bottom of the soil column and the surface displacement, with a comparison between the two-phase predictions and three-phase formulations considering permeability modifications. As can be seen, pore gas pressure evolves temporally, with great fluctuations when saturation-dependent permeability is active. The excess gas pressure influences liquid pressure and soil consolidation rate significantly. This underscores the importance of incorporating pore gas phase transport and permeability coupling to fully account for gas compressibility and mobility for accurate prediction of unsaturated soil behavior. The three-phase formulation with permeability adjustments also predicts slower consolidation, which is consistent with enhanced gas-phase resistance.

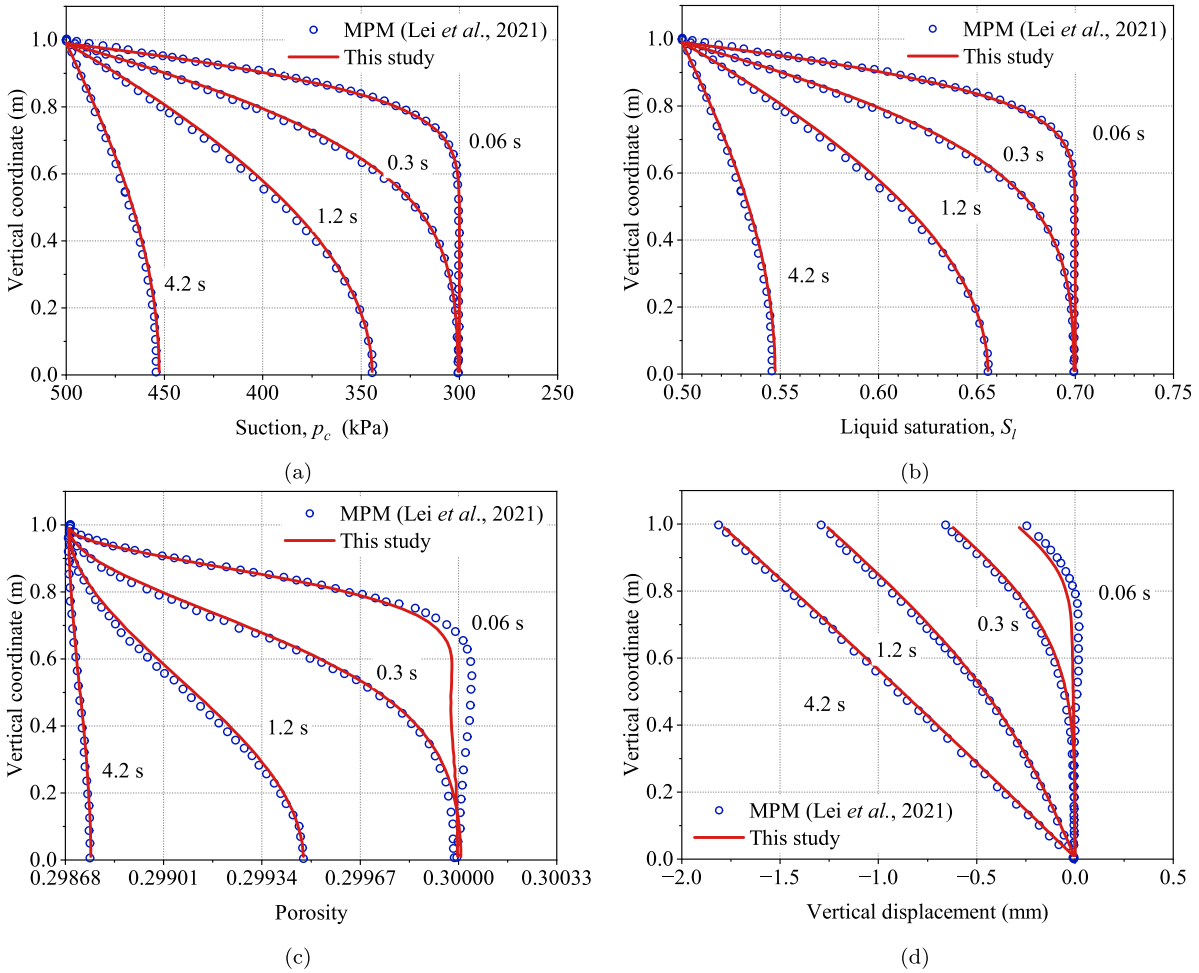

Fig. 29. Comparison of simulation results of the 1D unsaturated soil consolidation problem by the presented FSM-based MPM and explicit MPM in Lei et al. [23].

From Fig. 30, oscillations in gas pressure (Fig. 30(b)) and surface displacement (Fig. 30(d)) prompt an investigation into whether the three-phase formulation alters wave propagation patterns. To address this, we re-simulate the 1D consolidation case in Section 4.1.2 using the three-phase fractional step formulation, incorporating the following gas-phase properties: gas viscosity $\mu_g = 1\times10^{-5}$ Pa s, gas molar mass $M_g = 0.029$ kg/mol, and permeability $k_a = 1\times10^{-10}$ m^2. The compressibility for the fluid phase is set as $\alpha_l = 0.5\times10^{-9}$ Pa^{-1}. Initial conditions include initial liquid saturation $S_l = 0.9$, initial pore pressure at 100 kPa, and average gas–liquid system compressibility $\alpha_f \approx 1\times10^{-6}$ Pa^{-1}. The saturation-dependent permeability is not considered. The Van Genuchten (VG) model is adopted for the SWRC curve [66]:

$$p_c = p_0(S_e^{-1/m} - 1)^{1-m}, \tag{80}$$

where p_0 is the reference pressure and m is a material constant, taken as 100 kPa and 0.3, respectively. The VG model ensures the liquid saturation evolves within the physical range, *i.e.*, $(S_{lc}, 1]$. Fig. 31 shows the temporal evolution of pore liquid pressure, pore gas pressure, liquid saturation, and surface displacement, with the following observations. (1) Pressure waves persist in the three-phase system but dampen faster than in the two-phase formulations, likely due to energy dissipation from gas–liquid relative motion. (2) Gas pressure and liquid saturation exhibit transient fluctuations during consolidation before gradually returning to initial states as fluids equilibrate. (3) Gas-phase dynamics significantly influence transient consolidation rates but do not alter final soil settlement, highlighting their role in dynamics (vs. static) responses. This analysis confirms that the three-phase FSM effectively captures dynamic wave propagation in triphasic porous systems, demonstrating its adaptability for complex fluid–solid interactions. The enhanced damping mechanism underscores the importance of phase coupling in transient regimes, even when saturation-dependent permeability is neglected.

The above showcases the feasibility of extending the two-phase fractional step formulation to three-phase conditions, supported by preliminary validations and illustrative benchmarks. While the results underscore the method's potential for resolving dynamic

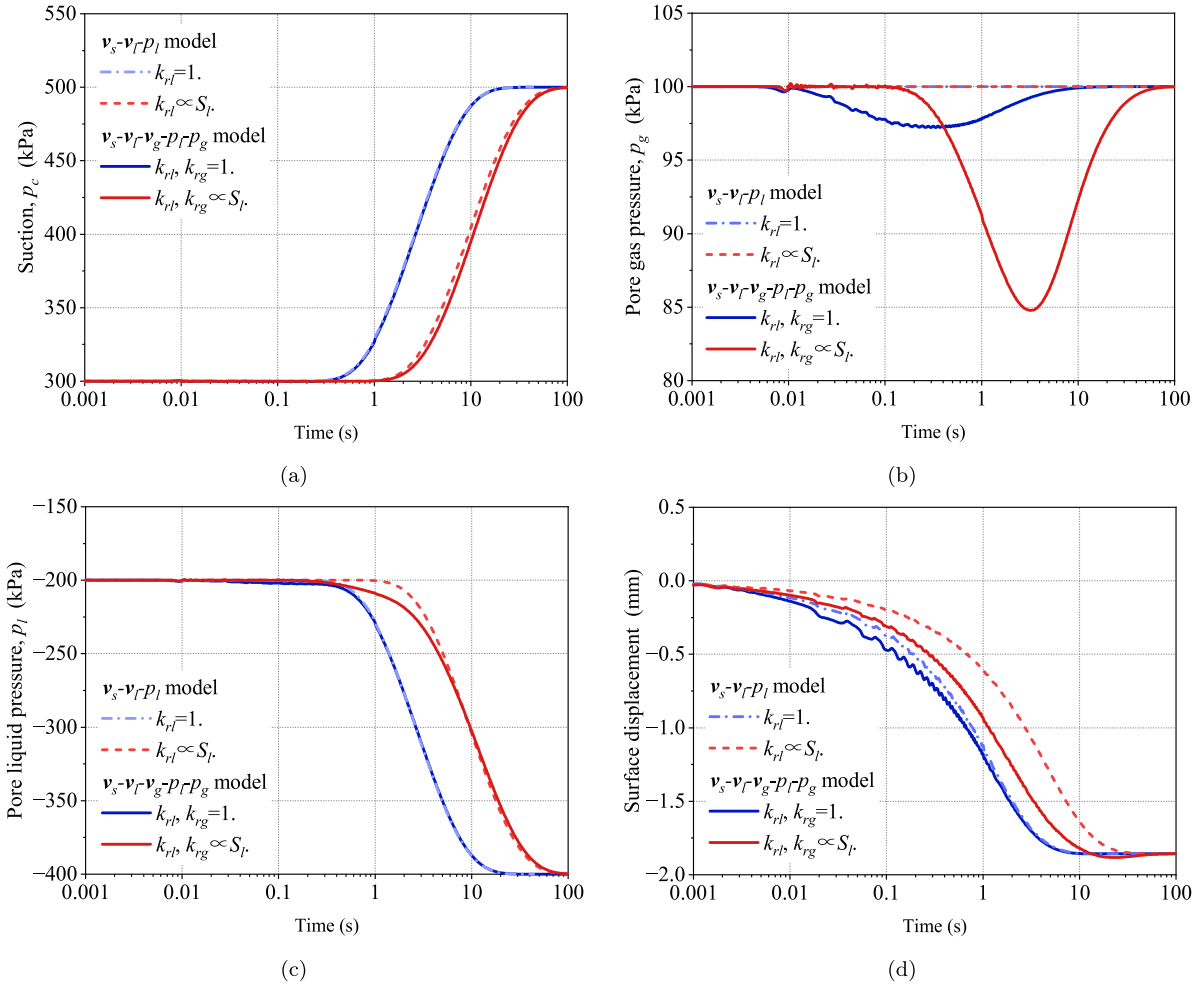

Fig. 30. Evolution of (a) suction, (b) pore gas pressure, and (c) pore liquid pressure at the bottom of the soil column, and (d) the surface displacement solved by two-phase or three-phase FSMs.

interactions in unsaturated media, comprehensive numerical implementation detail and rigorous validation of the three-phase FSM remain beyond the current scope.

6. Concluding remarks

Accurately simulating porous media often requires consideration of fluid compressibility, which becomes particularly significant when the fluid phase comprises a highly compressible fluid, such as unsaturated soils and gas hydrate-bearing sediments. This study presents an improved semi-implicit fractional step formulation in the material point method (MPM) for porous media, accounting for the compressibility of pore fluids under both isothermal and non-isothermal conditions. A series of validation tests is conducted to evaluate the performance of the FSM in capturing the key hydro-mechanical and thermo-hydro-mechanical responses involving compressible fluids. The main conclusions are summarized as follows:

Firstly, the semi-implicit FSM that considers compressible fluid can effectively capture pressure shock waves within porous media. In contrast, the original incompressible FSM fails to account for such dynamic effects, as it neglects the time-dependent pressure term in the continuity equation. However, accurate wave characteristics, including amplitude, length, and attenuation, can only be captured if the time increment is smaller than the critical time step related to undrained wave propagation; otherwise, the wave will be overdamped. Additionally, wave characteristics are closely related to fluid compressibility. For example, the same porous media with low fluid compressibility may produce higher-frequency and higher-amplitude pressure waves with faster wave attenuation, while a high fluid compressibility may yield the opposite effect. These findings are consistent with theoretical analyses based on Fourier Analysis [47]. Similar to mechanical loads, thermal loads can also generate pressure shocks due to instantaneous thermal expansion/contraction. Overall, this study demonstrates that the FSM-based semi-implicit MPM is versatile for various fluid conditions.

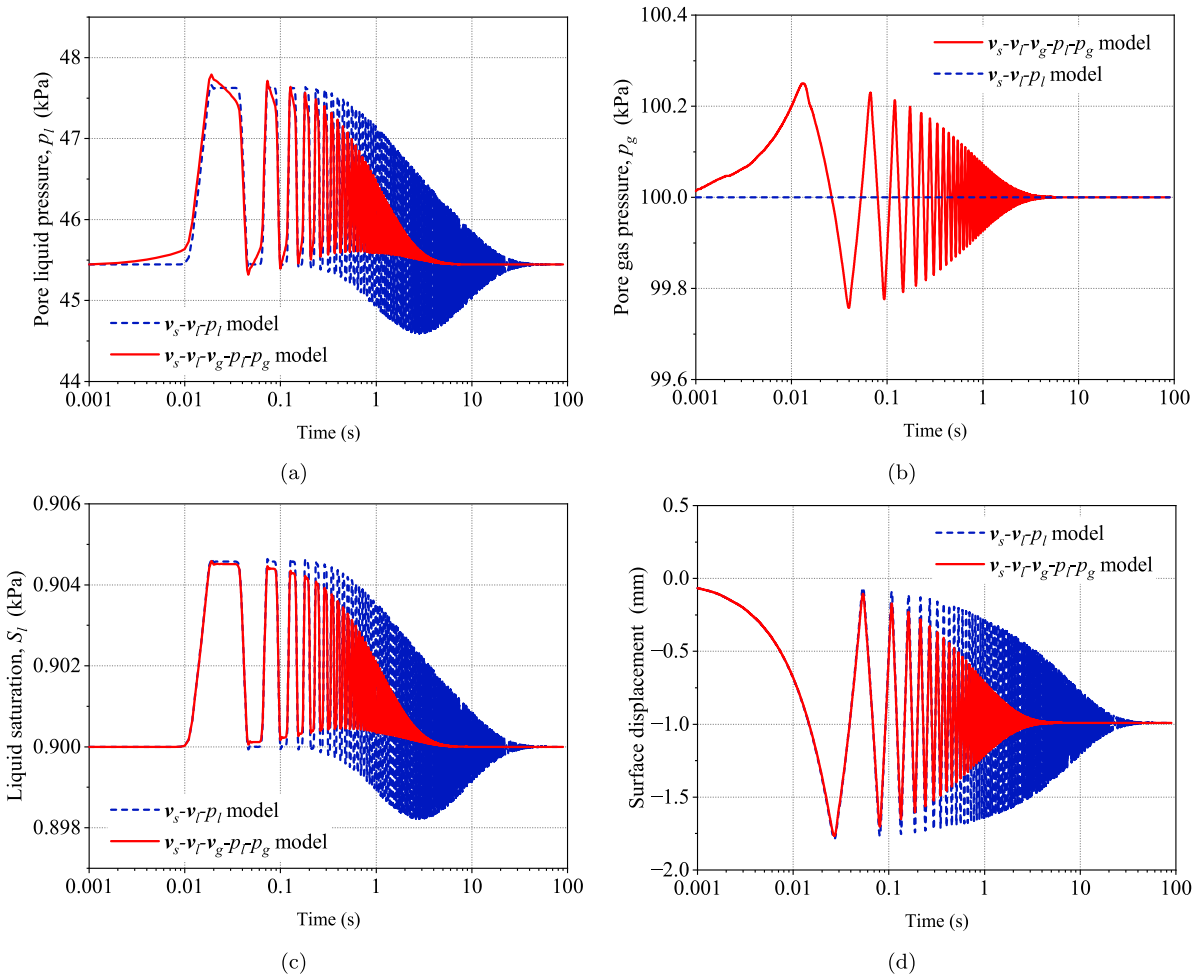

Fig. 31. Comparison of simulated wave propagation in 1D consolidation problem by three-phase FSM and simplified two-phase FSM.

Although the pressure wave and the wave propagation are inherent phenomena in fluid-infiltrated porous media, such dynamic effects may be undesirable in some scenarios, as wave reflection can contaminate results in the region of interest [39]. This is why one might opt to assume incompressibility for weakly compressible fluids, such as water. Alternatively, waves can be mitigated by introducing artificial damping or by implementing absorbing boundary conditions. Nevertheless, accounting for fluid and solid compressibility is crucial in many practical applications. Finally, we discussed the potential extension of the FSM for the real three-phase porous media, such as unsaturated soil, considering the capillary effect. Future work should focus on the rigorous validation and application of the three-phase FSM formulation for non-isothermal unsaturated conditions and multiphase gas–water flows in porous media.

CRediT authorship contribution statement

Jidu Yu: Writing – original draft, Visualization, Validation, Software, Methodology, Investigation, Formal analysis, Data curation, Conceptualization. **Weijian Liang:** Writing – review & editing, Validation, Methodology, Investigation, Formal analysis. **Jidong Zhao:** Writing – review & editing, Writing – original draft, Supervision, Resources, Project administration, Investigation, Funding acquisition, Formal analysis, Conceptualization.

Declaration of competing interest

The authors declare that they have no known competing financial interests or personal relationships that could have appeared to influence the work reported in this paper.

Acknowledgments

This work is financially supported by National Natural Science Foundation of China (Key Project #52439001), Research Grants Council of Hong Kong (GRF #16203123, GRF #16206322, CRF #C7082-22G, TRS #T22-607/24-N, TRS #T22-606/23-R).

Appendix. Matrices in three-phase fractional step formulation

The components of each matrix in the three-phase fractional step formulation in Section 5 are given as follows:

$$(\mathcal{M}_\pi)_I = \sum_{p=1}^{N_p} V_p n_{\pi p} \rho_{\pi p} S_{Ip},\ \pi = s, l, g, \tag{A.1a}$$

$$(\mathcal{Q}^d_\vartheta)_I = \sum_{p=1}^{N_p} V_p (\phi_p S_{\vartheta p})^2 \frac{\mu_{\vartheta p}}{k_{ap} k_{r\vartheta p}} S_{Ip},\ \vartheta = l, g, \tag{A.1b}$$

$$(\boldsymbol{f}^{int})_I = -\sum_{p=1}^{N_p} V_p \nabla S_{Ip} : \boldsymbol{\sigma}^k_p, \tag{A.1c}$$

$$(\boldsymbol{f}^{ext})_I = \sum_{p=1}^{N_p} V_p h_p^{-1} \hat{\boldsymbol{t}}_p S_{Ip} + \sum_{p=1}^{N_p} V_p \rho_{mp} \boldsymbol{b}_p S_{Ip}, \tag{A.1d}$$

$$(\boldsymbol{f}^{int}_\vartheta)_I = \sum_{p=1}^{N_p} V_p \phi_p S_{\vartheta p} p^k_{\vartheta p} \nabla S_{Ip}, \tag{A.1e}$$

$$(\boldsymbol{f}^{ext}_\vartheta)_I = \sum_{p=1}^{N_p} V_p h_p^{-1} \hat{\boldsymbol{t}}_{\vartheta p} S_{Ip} + \sum_{p=1}^{N_p} V_p \phi_p S_{\vartheta p} \rho_{\vartheta p} \boldsymbol{b}_p S_{Ip}, \tag{A.1f}$$

$$(\mathcal{L}_{\vartheta\vartheta})_{IJ} = \sum_{p=1}^{N_p} V_p \Delta t S_{\vartheta p} \left(\frac{1-\phi_p}{\rho_{sp}} S_{\vartheta p} + \frac{\phi_p}{\rho_{\vartheta p}} \right) S_{Ip} S_{Jp}, \tag{A.1g}$$

$$(\mathcal{L}_{lg})_{IJ} = (\mathcal{L}_{gl})_{IJ} = \sum_{p=1}^{N_p} V_p \Delta t S_{lp} S_{gp} \frac{1-\phi_p}{\rho_{sp}} S_{Ip} S_{Jp}, \tag{A.1h}$$

$$(\mathcal{K}_{\vartheta\vartheta})_{IJ} = \sum_{p=1}^{N_p} V_p (\Delta t)^{-1} \left(\phi_p S_{\vartheta p} \alpha_{\vartheta p} + \phi_p \frac{\partial S_{lp}}{\partial p_{lp}} \right) S_{Ip} S_{Jp}, \tag{A.1i}$$

$$(\mathcal{K}_{lg})_{IJ} = (\mathcal{K}_{gl})_{IJ} = -\sum_{p=1}^{N_p} V_p (\Delta t)^{-1} \phi_p \frac{\partial S_{lp}}{\partial p_{lp}} S_{Ip} S_{Jp}, \tag{A.1j}$$

$$(\mathcal{F}_{\vartheta\vartheta})_{IJ} = \sum_{p=1}^{N_p} V_p \phi_p S_{\vartheta p} \nabla S_{Ip} S_{Jp}, \tag{A.1k}$$

$$(\mathcal{F}_{\vartheta s})_{IJ} = -\sum_{p=1}^{N_p} V_p S_{\vartheta p} S_{Ip} \nabla S_{Jp}, \tag{A.1l}$$

$$(\mathcal{N}_{\vartheta\vartheta})_{IJ} = -\sum_{p=1}^{N_p} V_p \phi_p S_{\vartheta p} S_{Ip} \nabla S_{Jp}, \tag{A.1m}$$

$$(\mathcal{N}_{s\vartheta})_{IJ} = -\sum_{p=1}^{N_p} V_p (1-\phi_p) S_{\vartheta p} S_{Ip} \nabla S_{Jp}. \tag{A.1n}$$

Data availability

Data will be made available on request.

References

[1] K. Soga, E. Alonso, A. Yerro, K. Kumar, S. Bandara, Trends in large-deformation analysis of landslide mass movements with particular emphasis on the material point method, Géotechnique 66 (3) (2016) 248–273, http://dx.doi.org/10.1680/jgeot.15.LM.005.

[2] S. Idelsohn, E. Oñate, F.D. Pin, The particle finite element method: A powerful tool to solve incompressible flows with free-surfaces and breaking waves, Internat. J. Numer. Methods Engrg. 61 (7) (2004) 964–989, http://dx.doi.org/10.1002/nme.1096.

[3] W.-H. Yuan, M. Liu, X.-W. Zhang, H.-L. Wang, W. Zhang, W. Wu, Stabilized smoothed particle finite element method for coupled large deformation problems in geotechnics, Acta Geotech. (2022) http://dx.doi.org/10.1007/s11440-022-01691-6.

[4] D. Sulsky, S.-J. Zhou, H.L. Schreyer, Application of a particle-in-cell method to solid mechanics, Comput. Phys. Comm. 87 (1–2) (1995) 236–252.
[5] S. Bardenhagen, J. Brackbill, D. Sulsky, The material-point method for granular materials, Comput. Methods Appl. Mech. Engrg. 187 (3–4) (2000) 529–541, http://dx.doi.org/10.1016/S0045-7825(99)00338-2.
[6] S.G. Bardenhagen, E.M. Kober, The generalized interpolation material point method, Comput. Model. Eng. Sci. 5 (6) (2004) 477–496.
[7] H. Bui, R. Fukagawa, K. Sako, J. Wells, Slope stability analysis and discontinuous slope failure simulation by elasto-plastic smoothed particle hydrodynamics (SPH), Géotechnique 61 (7) (2011) 565–574, http://dx.doi.org/10.1680/geot.9.P.046.
[8] Y. Lian, H.H. Bui, G.D. Nguyen, S. Zhao, A. Haque, A computationally efficient SPH framework for unsaturated soils and its application to predicting the entire rainfall-induced slope failure process, Géotechnique (2022) 1–19, http://dx.doi.org/10.1680/jgeot.21.00349.
[9] G. Ma, H. Bui, Y. Lian, K. Tran, G. Nguyen, A five-phase approach, SPH framework and applications for predictions of seepage-induced internal erosion and failure in unsaturated/saturated porous media, Comput. Methods Appl. Mech. Engrg. 401 (2022) http://dx.doi.org/10.1016/j.cma.2022.115614.
[10] W.K. Liu, S. Jun, Y.F. Zhang, Reproducing kernel particle methods, Internat. J. Numer. Methods Fluids 20 (8–9) (1995) 1081–1106.
[11] W.K. Liu, Y. Chen, S. Jun, J.S. Chen, T. Belytschko, C. Pan, R.A. Uras, C.T. Chang, Overview and applications of the reproducing kernel particle methods, Arch. Comput. Methods Eng. 3 (1) (1996) 3–80, http://dx.doi.org/10.1007/BF02736130.
[12] S.A. Silling, M. Epton, O. Weckner, J. Xu, E. Askari, Peridynamic states and constitutive modeling, J. Elast. 88 (2) (2007) 151–184, http://dx.doi.org/10.1007/s10659-007-9125-1.
[13] C. Yang, F. Zhu, J. Zhao, Coupled total- and semi-Lagrangian peridynamics for modelling fluid-driven fracturing in solids, Comput. Methods Appl. Mech. Engrg. 419 (2024) 116580, http://dx.doi.org/10.1016/j.cma.2023.116580.
[14] X. Wang, Z.-Y. Yin, W. Wu, H.-H. Zhu, Differentiable finite element method with Galerkin discretization for fast and accurate inverse analysis of multidimensional heterogeneous engineering structures, Comput. Methods Appl. Mech. Engrg. 437 (2025) 117755, http://dx.doi.org/10.1016/j.cma.2025.117755.
[15] H.W. Zhang, K.P. Wang, Z. Chen, Material point method for dynamic analysis of saturated porous media under external contact/impact of solid bodies, Comput. Methods Appl. Mech. Engrg. 198 (17) (2009) 1456–1472, http://dx.doi.org/10.1016/j.cma.2008.12.006.
[16] I. Jassim, D. Stolle, P. Vermeer, Two-phase dynamic analysis by material point method, Int. J. Numer. Anal. Methods Geomech. 37 (15) (2013) 2502–2522, http://dx.doi.org/10.1002/nag.2146.
[17] S. Bandara, K. Soga, Coupling of soil deformation and pore fluid flow using material point method, Comput. Geotech. 63 (2015) 199–214, http://dx.doi.org/10.1016/j.compgeo.2014.09.009.
[18] J. Zhao, P. Zhang, X. Yang, J. Qi, On the uniaxial compression strength of frozen gravelly soils, Cold Reg. Sci. Technol. 171 (2020) 102965, http://dx.doi.org/10.1016/j.coldregions.2019.102965.
[19] S. Kularathna, W. Liang, T. Zhao, B. Chandra, J. Zhao, K. Soga, A semi-implicit material point method based on fractional-step method for saturated soil, Int. J. Numer. Anal. Methods Geomech. 45 (10) (2021) 1405–1436, http://dx.doi.org/10.1002/nag.3207.
[20] X. Zheng, F. Pisanò, P.J. Vardon, M.A. Hicks, An explicit stabilised material point method for coupled hydromechanical problems in two-phase porous media, Comput. Geotech. 135 (2021) 104112, http://dx.doi.org/10.1016/j.compgeo.2021.104112.
[21] N.M. Pinyol, M. Alvarado, E.E. Alonso, F. Zabala, Thermal effects in landslide mobility, Géotechnique 68 (6) (2018) 528–545, http://dx.doi.org/10.1680/jgeot.17.P.054.
[22] X. Lei, S. He, L. Wu, Stabilized generalized interpolation material point method for coupled hydro-mechanical problems, Comput. Part. Mech. 8 (4) (2021) 701–720, http://dx.doi.org/10.1007/s40571-020-00365-y.
[23] X. Lei, S. He, A. Abed, X. Chen, Z. Yang, Y. Wu, A generalized interpolation material point method for modelling coupled thermo-hydro-mechanical problems, Comput. Methods Appl. Mech. Engrg. 386 (2021) 114080, http://dx.doi.org/10.1016/j.cma.2021.114080.
[24] X. Zheng, F. Pisanò, P.J. Vardon, M.A. Hicks, Fully implicit, stabilised MPM simulation of large-deformation problems in two-phase elastoplastic geomaterials, Comput. Geotech. 147 (2022) 104771, http://dx.doi.org/10.1016/j.compgeo.2022.104771.
[25] W. Sun, A stabilized finite element formulation for monolithic thermo-hydro-mechanical simulations at finite strain, Internat. J. Numer. Methods Engrg. 103 (11) (2015) 798–839, http://dx.doi.org/10.1002/nme.4910.
[26] Y. Zhao, J. Choo, Stabilized material point methods for coupled large deformation and fluid flow in porous materials, Comput. Methods Appl. Mech. Engrg. 362 (2020) 112742, http://dx.doi.org/10.1016/j.cma.2019.112742.
[27] J. Choo, Stabilized mixed continuous/enriched Galerkin formulations for locally mass conservative poromechanics, Comput. Methods Appl. Mech. Engrg. 357 (2019) 112568, http://dx.doi.org/10.1016/j.cma.2019.112568.
[28] B. Chandra, R. Hashimoto, K. Kamrin, K. Soga, Mixed material point method formulation, stabilization, and validation for a unified analysis of free-surface and seepage flow, 2024, arXiv:2402.11719.
[29] B. Chandra, R. Hashimoto, S. Matsumi, K. Kamrin, K. Soga, Stabilized mixed material point method for incompressible fluid flow analysis, Comput. Methods Appl. Mech. Engrg. 419 (2024) 116644.
[30] W. Liang, J. Zhao, H. Wu, K. Soga, Multiscale, multiphysics modeling of saturated granular materials in large deformation, Comput. Methods Appl. Mech. Engrg. 405 (2023) 115871, http://dx.doi.org/10.1016/j.cma.2022.115871.
[31] J. Yu, J. Zhao, W. Liang, S. Zhao, A semi-implicit material point method for coupled thermo-hydro-mechanical simulation of saturated porous media in large deformation, Comput. Methods Appl. Mech. Engrg. 418 (2024) 116462, http://dx.doi.org/10.1016/j.cma.2023.116462.
[32] J. Yu, J. Zhao, W. Liang, S. Zhao, Multiscale modeling of coupled thermo-hydro-mechanical behavior in ice-bonded granular media subject to freeze-thaw cycles, Comput. Geotech. 171 (2024) 106349, http://dx.doi.org/10.1016/j.compgeo.2024.106349.
[33] J. Yu, J. Zhao, S. Zhao, W. Liang, Thermo-hydro-mechanical coupled material point method for modeling freezing and thawing of porous media, Int. J. Numer. Anal. Methods Geomech. 48 (13) (2024) 3308–3349, http://dx.doi.org/10.1002/nag.3794.
[34] W.-H. Yuan, H. Zheng, X. Zheng, B. Wang, W. Zhang, An improved semi-implicit material point method for simulating large deformation problems in saturated geomaterials, Comput. Geotech. 161 (2023) 105614, http://dx.doi.org/10.1016/j.compgeo.2023.105614.
[35] S. Hidano, Y. Yamaguchi, S. Takase, S. Moriguchi, K. Kaneko, K. Terada, Semi-implicit material point method for simulating infiltration-induced failure of unsaturated soil structures, Int. J. Numer. Anal. Methods Geomech. 48 (10) (2024) 2661–2699, http://dx.doi.org/10.1002/nag.3750.
[36] A. Chorin, Numerical solution of the Navier-Stokes equations, Math. Comp. 22 (104) (1968) 745–762.
[37] J.-L. Guermond, L. Quartapelle, On stability and convergence of projection methods based on pressure Poisson equation, Internat. J. Numer. Methods Fluids 26 (9) (1998) 1039–1053, http://dx.doi.org/10.1002/(SICI)1097-0363(19980515)26:9<1039::AID-FLD675>3.0.CO;2-U.
[38] J.L. Guermond, P. Minev, J. Shen, An overview of projection methods for incompressible flows, Comput. Methods Appl. Mech. Engrg. 195 (44) (2006) 6011–6045, http://dx.doi.org/10.1016/j.cma.2005.10.010.
[39] B. Markert, Y. Heider, W. Ehlers, Comparison of monolithic and splitting solution schemes for dynamic porous media problems, Internat. J. Numer. Methods Engrg. 82 (11) (2010) 1341–1383, http://dx.doi.org/10.1002/nme.2789.
[40] M. Huang, S. Wu, O.C. Zienkiewicz, Incompressible or nearly incompressible soil dynamic behaviour— a new staggered algorithm to circumvent restrictions of mixed formulation, Soil Dyn. Earthq. Eng. 21 (2) (2001) 169–179, http://dx.doi.org/10.1016/S0267-7261(00)00105-6.
[41] M. Huang, Z.Q. Yue, L.G. Tham, O.C. Zienkiewicz, On the stable finite element procedures for dynamic problems of saturated porous media, Internat. J. Numer. Methods Engrg. 61 (9) (2004) 1421–1450, http://dx.doi.org/10.1002/nme.1115.

[42] X. Li, X. Han, M. Pastor, An iterative stabilized fractional step algorithm for finite element analysis in saturated soil dynamics, Comput. Methods Appl. Mech. Engrg. 192 (35) (2003) 3845–3859, http://dx.doi.org/10.1016/S0045-7825(03)00378-5.
[43] J. Yu, J. Zhao, S. Zhao, W. Liang, Multiphysics simulation of freezing and thawing granular media using material point method, in: IOP Conference Series: Earth and Environmental Science, vol. 1330, no. 1, IOP Publishing, 2024, p. 012035.
[44] A. Yerro, E. Alonso, N. Pinyol, The material point method for unsaturated soils, Géotechnique 65 (3) (2015) 201–217, http://dx.doi.org/10.1680/geot.14.P.163.
[45] A. Yerro, V. Girardi, M. Martinelli, F. Ceccato, Modelling unsaturated soils with the material point method. A discussion of the state-of-the-art, Geomech. Energy Environ. 32 (2022) 100343, http://dx.doi.org/10.1016/j.gete.2022.100343.
[46] I. Lunati, P. Jenny, Multiscale finite-volume method for compressible multiphase flow in porous media, J. Comput. Phys. 216 (2) (2006) 616–636.
[47] A. Verruijt, Consolidation, Introd. Soil Mech. (2010) 123–129.
[48] K. Kumar, J. Salmond, S. Kularathna, C. Wilkes, E. Tjung, G. Biscontin, K. Soga, Scalable and modular material point method for large-scale simulations, 2019, arXiv:1909.13380 [Physics] arXiv:1909.13380.
[49] R.W. Lewis, B.A. Schrefler, The Finite Element Method in the Static and Dynamic Deformation and Consolidation of Porous Media, John Wiley & Sons, 1998.
[50] D.-Y. Peng, D.B. Robinson, A new two-constant equation of state, Ind. Eng. Chem. Fundam. 15 (1) (1976) 59–64.
[51] D. Gawin, B.A. Schrefler, M. Galindo, Thermo-hydro-mechanical analysis of partially saturated porous materials, Eng. Comput. 13 (7) (1996) 113–143, http://dx.doi.org/10.1108/02644409610151584.
[52] Z. Ye, L. Wang, B. Zhu, H. Shao, W. Xu, Y. Chen, A thermo-hydro-chemo-mechanical coupled model for natural gas hydrate-bearing sediments considering gravity effect, J. Nat. Gas Sci. Eng. 108 (2022) 104823, http://dx.doi.org/10.1016/j.jngse.2022.104823.
[53] K. Terzaghi, Theoretical Soil Mechanics, Chapman And Hall, Limited, London, 1951.
[54] M.A. Biot, General theory of three-dimensional consolidation, J. Appl. Phys. 12 (2) (1941) 155–164, http://dx.doi.org/10.1063/1.1712886.
[55] G.W.M. Peters, F.P.T. Baaijens, Modelling of non-isothermal viscoelastic flows, J. Non-Newton. Fluid Mech. 68 (2) (1997) 205–224, http://dx.doi.org/10.1016/S0377-0257(96)01511-X.
[56] J. Tao, H. Zhang, Y. Zheng, Z. Chen, Development of generalized interpolation material point method for simulating fully coupled thermomechanical failure evolution, Comput. Methods Appl. Mech. Engrg. 332 (2018) 325–342, http://dx.doi.org/10.1016/j.cma.2017.12.014.
[57] Z.-P. Chen, X. Zhang, K.Y. Sze, L. Kan, X.-M. Qiu, V-p material point method for weakly compressible problems, Comput. Fluids 176 (2018) 170–181, http://dx.doi.org/10.1016/j.compfluid.2018.09.005.
[58] K. Feng, G. Wang, D. Huang, F. Jin, Material point method for large-deformation modeling of coseismic landslide and liquefaction-induced dam failure, Soil Dyn. Earthq. Eng. 150 (2021) 106907, http://dx.doi.org/10.1016/j.soildyn.2021.106907.
[59] B.L. Aboustit, S.H. Advani, J.K. Lee, R.S. Sandhu, Finite element evaluations of thermo-elastic consolidation, in: The 23rd U.S Symposium on Rock Mechanics (USRMS), OnePetro, 1982.
[60] J. Noorishad, C.F. Tsang, P.A. Witherspoon, Coupled thermal-hydraulic-mechanical phenomena in saturated fractured porous rocks: numerical approach, J. Geophys. Res.: Solid Earth 89 (B12) (1984) 10365–10373, http://dx.doi.org/10.1029/JB089iB12p10365.
[61] R.W. Lewis, C.E. Majorana, B.A. Schrefler, A coupled finite element model for the consolidation of nonisothermal elastoplastic porous media, Transp. Porous Media 1 (2) (1986) 155–178, http://dx.doi.org/10.1007/BF00714690.
[62] W. Cui, K.A. Gawecka, D.M. Potts, D.M.G. Taborda, L. Zdravković, A Petrov-Galerkin finite element method for 2D transient and steady state highly advective flows in porous media, Comput. Geotech. 100 (2018) 158–173, http://dx.doi.org/10.1016/j.compgeo.2018.04.013.
[63] R. Wu, Analytical Study on One-Dimensional Thermal Consolidation Theory of Saturated Soil (Ph.D. thesis), Zhejiang University, 2008.
[64] S. Zhao, J. Zhao, Y. Lai, Multiscale modeling of thermo-mechanical responses of granular materials: a hierarchical continuum– discrete coupling approach, Comput. Methods Appl. Mech. Engrg. 367 (2020) 113100, http://dx.doi.org/10.1016/j.cma.2020.113100.
[65] R.H. Brooks, Hydraulic Properties of Porous Media, Colorado State University, 1965.
[66] M.T. Van Genuchten, A closed-form equation for predicting the hydraulic conductivity of unsaturated soils, Soil Sci. Am. J. 44 (5) (1980) 892–898, http://dx.doi.org/10.2136/sssaj1980.03615995004400050002x.